

Control of a Permanent Magnet Synchronous Motor with Non-Sinusoidal Flux Density Distribution

OSKAR WALLMARK

Department of Electric Power Engineering
CHALMERS UNIVERSITY OF TECHNOLOGY
Göteborg, Sweden 2001

THESIS FOR THE MASTER OF SCIENCE DEGREE

**Control of a Permanent Magnet
Synchronous Motor with
Non-Sinusoidal Flux Density
Distribution**

OSKAR WALLMARK



Department of Electric Power Engineering
CHALMERS UNIVERSITY OF TECHNOLOGY
Göteborg, Sweden 2001

Control of a Permanent Magnet Synchronous Motor with Non-Sinusoidal Flux Density Distribution

Oskar Wallmark

© Oskar Wallmark, 2001.

Technical Report No. 59E
Department of Electric Power Engineering
CHALMERS UNIVERSITY OF TECHNOLOGY
SE-412 96 Göteborg
Sweden
Telephone + 46 (0)31 772 1000

Chalmers Reproservice
Göteborg, Sweden 2001

Abstract

This thesis discusses various aspects of controlling a permanent magnet synchronous machine with a non-sinusoidal rotor flux density distribution. The transient model of the machine in the rotor oriented dq -frame is derived, including the non-sinusoidal effects.

The design of current and speed controllers is also discussed. The current controller is implemented in a permanent magnet machine, intended for hybrid electric vehicle applications, yielding good results. An algorithm to estimate the rotor position, based on high frequency signal injection and a non linear observer, is also implemented with good results. The flux linkage harmonics are measured and the predicted torque and current ripple are verified by measurements.

Keywords: *Current control, non-sinusoidal flux density, permanent magnet, sensorless control, signal injection, speed control, synchronous machine, torque ripple.*

Acknowledgements

Many people have contributed to this thesis. I would like to thank my examiner Assoc. Prof. Ola Carlson for help with proofreading, financing and many other things concerning the project. I am very grateful to my main supervisor Tech. Lic. Rolf Ottersten for numerous fruitful discussions and invaluable help down in the laboratory. I would also like to thank Assoc. Prof. Torbjörn Thiringer for helping me with the measurement system and Prof. Lennart Harnefors for sharing with me his work and interesting discussions about control of electrical drives.

The financial support from the Swedish National Energy Administration is gratefully acknowledged.

Finally, I would like to thank the whole department for making me feel welcome and for the nice working atmosphere.

Oskar Wallmark
14th December 2001

Contents

Abstract	i
Acknowledgements	ii
Contents	iii
List of Symbols	v
I Introduction	1
1 The Hybrid Electric Vehicle Concept	2
1.1 Electrical Machines for Hybrid Electric Vehicle Applications	3
1.1.1 Permanent Magnet Synchronous Machines	3
1.1.2 Controlling the Machine	4
1.1.3 Torque Ripple in Permanent Magnet Synchronous Machines	5
1.2 Previous Work at the Department	6
II Theory	7
2 Transient Model of the Permanent Magnet Synchronous Machine	8
2.1 Modelling Non-Sinusoidal Flux Distribution	10
2.2 Mechanical Dynamics	13
2.2.1 The Electrical Torque Expression	13
2.3 Summary of the Transient Model	14
2.4 Steady State Model	15
3 Design of Current Controllers	16
3.1 Design of Current Controllers Using Internal Model Control	17
3.1.1 Selection of Active Damping	18
3.1.2 Summary of Current Controller Design	19
3.1.3 Torque Ripple Minimization with the IMC Current Controller	19
3.2 A Torque Ripple Minimization Technique Based on Amplitude and Phase Error Estimation	20

4	Design of the Speed Controller	24
4.1	Summary of Speed Controller Design	25
5	Sensorless Control of the Machine using Saliency	26
5.1	A Non linear Observer for Estimation of Rotor Angle and Rotor Speed . . .	28
III	Implementations	29
6	Measurement of Flux Linkage Harmonics	30
7	Implementation of the Current Controller	33
7.1	Step in i_q	33
7.1.1	Approximation of Moment of Inertia and Friction Torque	34
7.1.2	Simulation of the Machine	35
7.2	Implementation of the Sensorless Algorithm	36
7.2.1	Step in i_q	36
8	Measurement of Torque and Current Ripple	39
8.1	No Load Measurement	39
8.2	Small Load Measurement	40
9	Conclusions	43
9.1	Further Work	43
A	Calculation of Electrical Power in $dq0$-coordinates	48
B	Selection of γ Parameters for the MIT Update Rule	49
C	Laboratory Setup Data	51
D	Pictures of Laboratory Setup	53

List of Symbols

Abbreviations

diag	Diagonal matrix
DSP	Digital Signal Processor
EV	Electric Vehicle
FFT	Fast Fourier Transform
HEV	Hybrid Electric Vehicle
ICE	Internal Combustion Engine
IGBT	Insulated Gate Bipolar Transistor
IM	Induction Machine
IMC	Internal Model Control
PI	Proportional, Integral controller
PMSM	Permanent Magnet Synchronous Machine
PWM	Pulse Width Modulation
VSI	Voltage Source Inverter

Symbols

A, B, C	Meaning Matrix or vector
a, b, c	Matrix or vector
<u>A</u> , <u>B</u> , <u>C</u>	Phasor quantity
E	Back-emf vector
F	Controller transfer function matrix
<i>G</i>	Transfer function
G	Transfer function matrix
L	Inductance matrix
R	Resistance matrix
Ψ	Flux linkage vector

Superscript

ref	Meaning Reference value
-----	-----------------------------------

Subscript

<i>a, b, c</i>	Meaning Phase quantities
<i>cl</i>	Closed loop
<i>d</i>	Direct axis quantity

dist	Disturbance
dq	Vector or matrix containing d -, and q -component
$dq0$	Vector or matrix containing d -, q - and zero component
ph	Phase quantity
plant	Plant model
q	Quadrature axis quantity
0	Zero component quantity

Variable	Meaning	Unit
f_e	Frequency of injected signal	Hz
l_s	Length of stator	m
n_p	Number of pole pairs	–
r_s	Inner radius of stator	m
s	Laplace variable	–
$t_{r,c}$	Current rise time	s
$t_{r,s}$	Speed rise time	s
B_{fric}	Friction coefficient	Nm
B_r	Radial flux density	T
J	Moment of inertia	kgm ²
L_d	Direct axis inductance	H
L_q	Quadrature axis inductance	H
N_c	Number of coils in stator winding for each phase	–
P_e	Electrical power	W
$R_{a,d}$	d -axis active damping resistance	Ω
$R_{a,q}$	q -axis active damping resistance	Ω
R_s	Resistance per phase in stator winding	Ω
T_e	Electrical torque	Nm
T_{fric}	Friction torque	Nm
T_l	Load torque	Nm
V	Amplitude of injected voltage	V
X_d	Direct axis reactance	Ω
X_q	Quadrature axis reactance	Ω
α_c	Bandwidth of current controller	s ⁻¹
α_s	Bandwidth of speed controller	s ⁻¹
δ	Power angle	rad
θ	Rotor position	rad
$\hat{\theta}$	Estimated rotor position	rad

$\tilde{\theta}$	Estimated rotor position error	rad
$\tilde{\theta}_{max}$	Maximum allowed position estimation error	rad
ρ	Pole position of non linear observer	–
τ_m	Magnetic pole pitch	rad
φ	Phase angle	rad
$\hat{\varphi}$	Estimated phase angle	rad
ω_e	Injected signal frequency	rad/s
ω_m	Mechanical rotor speed	rad/s
ω_r	Electrical rotor speed	rad/s
$\Delta\omega_{ref}$	Maximum change of speed reference	rad/s

Part I

Introduction

Chapter 1

The Hybrid Electric Vehicle Concept

The idea of an electrical powered vehicle (EV) has been around for almost 200 years. The first electric vehicle was built by Thomas Davenport in 1834. Until a few decades ago, batteries seemed to be the only device capable of storing the energy in a safe manner. Unfortunately batteries are still not able to store the amount of energy needed to fulfill the needs of an electric vehicle completely. They also have a low energy to weight ratio and problems with the recharging of the battery are not completely solved. Currently a lot of research is focused on the possibility of using fuel cells for producing energy from hydrogen. Results are promising and fully functioning fuel cells may be the missing link that will make the EV a competitive alternative to the standard internal combustion engine (ICE) that is used in today's cars.

The customers' demand for an alternative to the combustion engine is, nonetheless, great. The environmental advantages of low emission and the possibility of using clean energy sources (like wind or hydro power) together with different forms of governmental support (environmental taxes, etc.) has forced the vehicle industry to look for an alternative to the electric vehicle. In the mid 90s, vehicle manufactures turned their attention back to hybrid electric vehicles (HEV) (the HEV concept is not new and the first patent involving HEV technology was filed in 1905 by the American H. Piper [32]). The change of focus to hybrid technology was done by almost all vehicle manufacturers. Many prototypes and a few mass produced vehicles are now available¹.

Like all modern cars, the hybrid electric vehicle is a complex object and research on HEVs is divided into many areas. Four different parts distinguish the hybrid electric vehicle from a standard combustion engine driven car. They are:

- A device to store a large amount of electrical energy.
- An electrical machine to convert electrical power into mechanical torque on the wheels.
- A modified internal combustion engine adapted to hybrid electric vehicle use.
- A transmission system between the two different propulsion techniques.

¹For example, there were 23 hybrid electric vehicles presented at the North American International Auto Show (NAIAS) in 2000 [33].

As pointed out above, the device for storing electrical energy could be batteries or hydrogen powered fuel cells. The storage need of electrical energy can vary a lot between a HEV and an EV since the HEV can use the electrical machine to act as a generator and thereby produce electrical energy, which can be stored and used later. A short discussion of which type of electrical machine that is used is found in Section 1.1. The combustion engine must of course also be designed for hybrid electric use. The transmission system between the combustion engine and the electrical machine is typically of series or parallel type (or variants thereof). Much research effort is being put into determining which of the two transmission systems is optimal.

1.1 Electrical Machines for Hybrid Electric Vehicle Applications

As mentioned above, the hybrid electric vehicle needs an electrical machine to transform electrical power to mechanical torque on the wheels. The electrical machine needs to be controlled accurately (control of speed and/or torque) and the only machine that initially could fulfill these demands was the DC motor [34]. Due to high weight and a short lifetime the DC motor was gradually replaced by the induction machine (IM). The induction machine is a robust, well-known device and, with the development of new power electronics (like the IGBT transistor), many new methods of controlling three phase machines have been developed. The induction machine is still used in many HEV concepts.

In order to increase the energy efficiency of the HEV, all parts of it have to be very efficient and, as an alternative, machines of the permanent magnet type have become a serious challenger to the IM. Recent research has also shown that the reluctance machine can be used in hybrid electric vehicles with good results [14, 24, 28]. The advantages of the reluctance machine are that it can be made smaller than the IM and cheaper than machines of the permanent magnet type due to the high cost of the permanent magnets.

1.1.1 Permanent Magnet Synchronous Machines

The permanent magnet synchronous machine (PMSM) is primarily associated with high performance applications and is normally fed by a voltage source inverter (VSI). The machine is of the synchronous type and the rotor field is created by permanent magnets attached to the rotor. The material of the permanent magnets can differ but the best materials are of rare earth type, such as Samarium-Cobalt (Sm-Co) or Neodymium-Iron-Boron (NeFeB) [18]. The NeFeB magnets combine a high flux density with a large coercive force. Unfortunately, they are still quite expensive but the price has dropped during the last decade.

The advantage of using permanent magnets in the rotor circuit is that the design of the machine is simplified and that there are virtually no losses in the rotor circuit since the rotor is (ideally) free of currents. The latter property is very attractive to the designer of electrical machines intended for HEV use since it reduces the losses and, thereby, increases the possible range of action for the vehicle.

The stator winding can be wound in several ways. Machines with trapezoidally wound stator windings are called brushless DC machines and should be fed by trapezoidal

currents to produce a smooth torque. Another winding method is to wind the stator sinusoidally. The combination of a sinusoidally wound stator and a permanent magnet rotor design is the basis of the permanent magnet synchronous machine.

The distribution of the magnets in the rotor can vary significantly. How the magnets are distributed, of course, affects the flux density field in the air gap. The ideal flux density field is sinusoidally formed, which will be shown in Section 2. Unfortunately this increases the complexity and cost of the machine. Many rotor designs try to approximate the sinusoidally flux density field.

1.1.2 Controlling the Machine

Methods for controlling PMSM drives, connected to different types of converters, have been developed both for steady state operation and high performance servo control. This thesis discusses the servo control of the PMSM but a small discussion of the steady state behaviour of the machine can be found in Section 2.4.

The most advanced type of control of electrical machines is known as *vector control*. The term *vector control* includes many different control methods but they all use different types of feedback mechanisms for improved control. The standard laboratory setup of a vector controlled PMSM is shown in Figure 1.1.

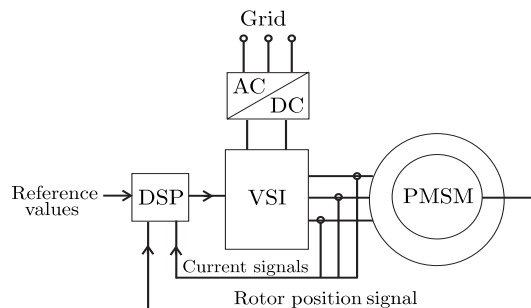


Figure 1.1: Basic principle of vector control.

The PMSM is fed by the voltage source inverter (VSI), which is powered by the grid through an AC/DC converter. For the hybrid electric case, the VSI is fed by a DC source, such as batteries. The VSI is controlled by a digital signal processor (DSP). A combination of a fast DSP and a modern VSI can control the voltage in the three phases of the PMSM very accurately. Note also the feedback devices, which consist of current measuring devices and rotor position detection. The rotor position detection usually consists of Hall sensors or a resolver. The term *sensorless control* usually implies that the rotor position and/or rotor speed is not measured but estimated from the currents fed to the machine. Using vector control, various parameters can be controlled, for example rotor speed, angular position and torque on the shaft. The torque on the shaft is controller in hybrid electric vehicle applications.

1.1.3 Torque Ripple in Permanent Magnet Synchronous Machines

The permanent magnet synchronous machine offers many advantages, such as high efficiency, low inertia and a high torque-to-volume ratio. The major drawback of the machine type is (apart from the high price of the magnets) the ripple in the produced torque. The sensitivity of torque ripple, of course, depends on the application. If the machine is used in a pump system, the torque ripple is of no importance. In other applications, the amount of torque ripple is critical. For example, the quality of the surface finish of a metal working machine is directly dependent on the smoothness of the delivered torque [15]. In a hybrid vehicle application, torque ripple could be a vibration or noise producing source which in the worst case could affect the exhaustion of active parts in the vehicle.

Torque ripple produced by a PMSM comes from two different sources. The first one is known as *cogging torque*. Cogging torque is generated by the interaction of the rotor magnetic flux and angular variations in the stator magnetic reluctance [15]. Different methods for reducing cogging torque exist and they mostly rely on changes in the design of the machine. One usual design method is known as *skewing*, which can be done on both the rotor and stator. Skewing can reduce the cogging torque very effectively but the manufacturing procedure is complicated, which increases the price of the machine [1]. Another drawback of skewing is that it decreases the average torque produced by the machine [15]. Other design methods for reducing cogging torque include shifting the permanent magnets, notching the stator teeth and using different pole arc widths [15, 19].

The second torque ripple source is generated by the interaction of the stator current magnetomotive forces and the magnetic field produced by the rotor. This torque, naturally, depends on both the construction of the stator and the rotor field. Different winding methods (like using short-pitched windings or fractional-slot-pitched windings) can reduce torque ripple. In order to minimize torque ripple, the rotor field produced by the magnets has to be sinusoidal. A sinusoidal field is, unfortunately, hard to manufacture since the design of the rotor magnets are complex and, thus, make the machine more expensive.

Control Methods for Reducing Torque Ripple

So far only design methods for reducing torque ripple have been discussed. The other method for reducing torque ripple in an existing machine is to use control schemes that reduce torque ripple. The basic goal of these control schemes is to control the current so that the ripple is cancelled out (this is known as *harmonic injection*). These methods have been applied for the last two decades. The shape of the injected current is not uniquely determined and an additional constraint is often added (to minimize ohmic losses, for example) [4, 22]. The shape of the ideal current, which minimizes torque ripples usually sets high demands on the current controller used. Holtz et al. use a predictive deadbeat current controller, which can control the current very accurately [13, 30]. The parameters of the current controller proposed by Holtz must be accurately set and a self-commissioning scheme is developed to identify the machine parameters [13]. Knowing the parameters well is of importance for all methods developed. Petrović et al. control the machine using an adaptive speed controller, which identifies the back-emf harmonics produced by the non-sinusoidal rotor field during operation [27].

1.2 Previous Work at the Department

A permanent magnet synchronous machine and voltage source inverter, suitable for HEV applications, have been designed and constructed at the department by Tech. Lic Johan Helsing and Tech. Lic Joachim Linström. The machine has four rotor poles of salient type and is water cooled. Data and pictures of the machine and inverter can be found in Appendix C-D. Since the machine is intended for HEV applications it has a very high energy efficiency. The maximum measured efficiency, in steady state, is approximately 95.5% [20]. For a complete description of the machine and inverter see [12, 20].

Part II

Theory

Chapter 2

Transient Model of the Permanent Magnet Synchronous Machine

In many textbooks treating transient phenomena of electrical machines, the permanent magnet synchronous machine is often treated as a special case of the electrically excited synchronous machine [26, 29]. It is almost always assumed that the flux linkage¹ is sinusoidally distributed [2, 18, 26, 29, 31]. Since this thesis focuses only on the permanent magnet synchronous machine with non-sinusoidal flux distribution, an accurate derivation of its transient model is needed. The following derivation is based on these four assumptions:

- The stator winding is sinusoidally distributed around the periphery of the air gap.
- The effect of stator slots on the rotor angle dependence of the inductances is neglected.
- Linear magnetic conditions (no saturation).
- No temperature or frequency dependence of the resistances and inductances.

Since the stator winding is sinusoidally distributed, the three phases can be represented as three *phase vectors*, f_a , f_b and f_c , which could be either current or voltages. The phase vectors are fixed in direction with the angle $2\pi/3$ between them (note that the direction of the phase vectors is fixed but the amplitude of each vector may vary independently of the other ones). Figure 2.1 shows the phase vectors and the dq -coordinate system which is fixed to the rotor position (θ is the angle between f_a and the rotor position in electrical radians).

¹In this derivation the term flux is used instead of flux linkage in order to save space.

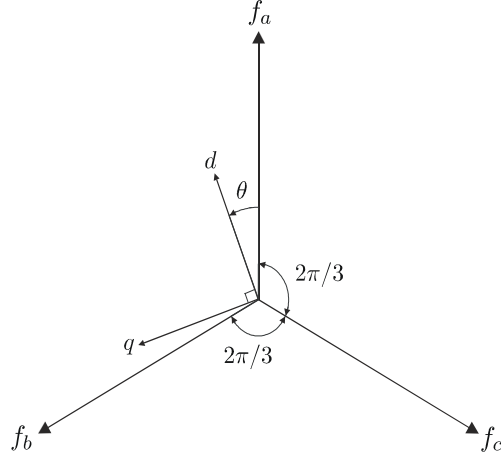


Figure 2.1: The phase vectors and the dq -coordinate system.

To transform the phase vectors to the dq -coordinate system we use the following equations:

$$f_d = K [f_a \cos \theta + f_b \cos(\theta - 2\pi/3) + f_c \cos(\theta + 2\pi/3)], \quad (2.1)$$

$$f_q = -K [f_a \sin \theta + f_b \sin(\theta - 2\pi/3) + f_c \sin(\theta + 2\pi/3)]. \quad (2.2)$$

We choose $K = \frac{2}{3}$ which yields an amplitude invariant transformation. In order to set up a transformation matrix of these equations, a third equation is needed since the right sides of Equations (2.1)–(2.2) contain three unknowns. We, therefore, introduce the zero-sequence equation

$$f_0 = \frac{1}{3} (f_a + f_b + f_c). \quad (2.3)$$

Now the matrix formulation of equations (2.1)–(2.3) can be written as

$$\underbrace{\begin{bmatrix} f_d \\ f_q \\ f_0 \end{bmatrix}}_{\mathbf{f}_{dq0}} = \frac{1}{3} \underbrace{\begin{bmatrix} 2 \cos \theta & 2 \cos(\theta - \frac{2\pi}{3}) & 2 \cos(\theta + \frac{2\pi}{3}) \\ -2 \sin \theta & -2 \sin(\theta - \frac{2\pi}{3}) & -2 \sin(\theta + \frac{2\pi}{3}) \\ 1 & 1 & 1 \end{bmatrix}}_{\mathbf{T}_{dq,ph}} \underbrace{\begin{bmatrix} f_a \\ f_b \\ f_c \end{bmatrix}}_{\mathbf{f}_{ph}}. \quad (2.4)$$

$\mathbf{T}_{dq,ph}$ is known as the *Blondel-Park-transformation matrix*. The inverse can be written as

$$\mathbf{T}_{dq,ph}^{-1} = \mathbf{T}_{ph,dq} = \begin{bmatrix} \cos \theta & -\sin \theta & 1 \\ \cos(\theta - \frac{2\pi}{3}) & -\sin(\theta - \frac{2\pi}{3}) & 1 \\ \cos(\theta + \frac{2\pi}{3}) & -\sin(\theta + \frac{2\pi}{3}) & 1 \end{bmatrix}. \quad (2.5)$$

2.1 Modelling Non-Sinusoidal Flux Distribution

The assumed radial flux density, $B_r(\theta)$, is shown in Figure 2.2 [12].

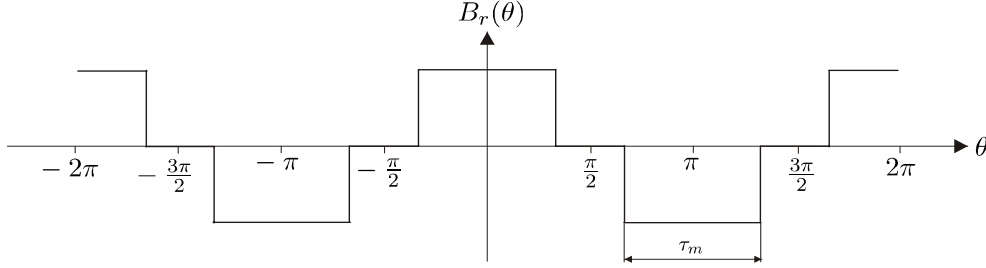


Figure 2.2: The assumed radial flux density in the air gap.

Here τ_m is the *magnetic pole pitch* expressed in electrical radians ($\tau_m = 0.65\pi$ for the machine at the department [12]). $B_r(\theta)$ can be expanded into a Fourier series as

$$B_r(\theta) = \sum_{i=1}^{\infty} B_{(2i-1)} \cos [(2i-1)\theta] = B_1 \cos \theta + B_3 \cos(3\theta) + B_5 \cos(5\theta) + \dots \quad (2.6)$$

The analytic calculation of the Fourier coefficients yields $B_i = \frac{4\hat{B}}{\pi i^2} \sin(i\tau_m/2)$, where $\hat{B} = B_m(0)$. We can see that the magnitude of the coefficients decreases rapidly with increased i . To calculate the flux induced in one phase, we assume that the stator winding is of *partial uniform distribution form* [29]. This means that each phase winding is distributed over an angle β with constant turn density (see Figure 2.3). For a two pole machine (which the derivation is based on) $\beta = 2\pi/3$.

To calculate the induced flux in phase a we use the standard form $\Psi = \int_{\mathbf{s}} \mathbf{B} \cdot d\mathbf{s}$. Since we have assumed a radial distribution of the flux density field this flux can be calculated as

$$\begin{aligned} \Psi_{m,a}(\theta) &= k \sum_{j=1}^{N_c} \left[\int_{\theta-\alpha_j/2}^{\theta+\alpha_j/2} B_r(\theta') r_s l_s d\theta' \right] \\ &= k \sum_{j=1}^{N_c} \left[\int_{\theta-\alpha_j/2}^{\theta+\alpha_j/2} r_s l_s \left(\sum_{i=1}^{\infty} B_{(2i-1)} \cos [(2i-1)\theta'] d\theta' \right) \right] \\ &= k r_s l_s \sum_{j=1}^{N_c} \sum_{i=1}^{\infty} \left[\int_{\theta-\alpha_j/2}^{\theta+\alpha_j/2} B_{2i-1} \cos [(2i-1)\theta'] d\theta' \right]. \end{aligned} \quad (2.7)$$

Here N_c is the number of coils in the stator winding for phase a and α_j is defined in Figure 2.3. r_s is the inner radius of the stator and l_s is the length of the stator. k is an arbitrary constant, which depends on the specific design of the stator. Evaluating the integral yields

$$\Psi_{m,a}(\theta) = 2kr_s l_s \sum_{j=1}^{N_c} \sum_{i=1}^{\infty} \left[\sin [(2i-1)\alpha_j/2] \frac{B_{(2i-1)} \cos [(2i-1)\theta]}{(2i-1)} \right]. \quad (2.8)$$

The important conclusion that can be drawn from Equation (2.8) is:

The induced flux linkage from the rotor magnets in the stator winding can also be expressed as a sum of odd cosines where the coefficients decrease rapidly.

$$\Psi_{m,a}(\theta) = \sum_{i=1}^{\infty} \Psi_{(2i-1)} \cos [(2i-1)\theta] = \psi_1 \cos \theta + \psi_3 \cos(3\theta) + \psi_5 \cos(5\theta) + \dots \quad (2.9)$$

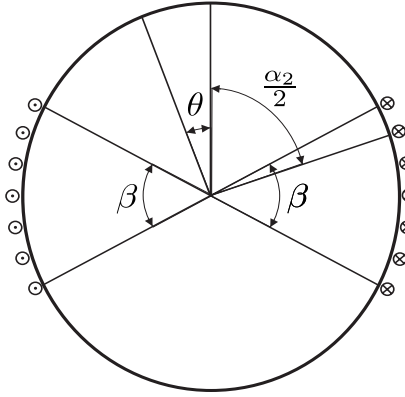


Figure 2.3: Simplified model of the stator winding for phase a .

From the geometry in Figure 2.1 we can see that the flux induced in each phase from the rotor magnets ($\Psi_{m,a}(\theta)$, $\Psi_{m,b}(\theta)$ and $\Psi_{m,c}(\theta)$) can be written as

$$\begin{bmatrix} \Psi_{m,a}(\theta) \\ \Psi_{m,b}(\theta) \\ \Psi_{m,c}(\theta) \end{bmatrix} = \begin{bmatrix} \Psi_{m,a}(\theta) \\ \Psi_{m,a}(\theta - 2\pi/3) \\ \Psi_{m,a}(\theta + 2\pi/3) \end{bmatrix} = \mathbf{\Psi}_{m,ph}. \quad (2.10)$$

We now transform $\mathbf{\Psi}_{m,ph}$ to the $dq0$ -coordinate system using Equation (2.4). Performing this quite tedious calculation yields (note the change of variable names in the last step)

$$\begin{aligned} \mathbf{\Psi}_{m,dq0} &= \mathbf{T}_{dq,ph} \mathbf{\Psi}_{m,ph} = \begin{bmatrix} \psi_1 + (\psi_5 + \psi_7) \cos(6\theta) + (\psi_{11} + \psi_{13}) \cos(12\theta) + \dots \\ (-\psi_5 + \psi_7) \sin(6\theta) + (-\psi_{11} + \psi_{13}) \sin(12\theta) + \dots \\ \psi_3 \cos(3\theta) + \psi_9 \cos(9\theta) + \psi_{15} \cos(15\theta) + \dots \end{bmatrix} \\ &= \begin{bmatrix} \psi_m + \psi_{d6} \cos(6\theta) + \psi_{d12} \cos(12\theta) + \dots \\ \psi_{q6} \sin(6\theta) + \psi_{q12} \sin(12\theta) + \dots \\ \psi_{03} \cos(3\theta) + \psi_{09} \cos(9\theta) + \dots \end{bmatrix}. \end{aligned} \quad (2.11)$$

It is important to note that Equation (2.11) is valid only for this choice of the Blondel-Park transformation matrix $\mathbf{T}_{dq,ph}$. Sometimes $\mathbf{T}_{dq,ph}$ is defined with a positive sign on

the second row (se Equation (2.4)). This means that the second row in Equation (2.11) will also change signs (the last term of Equation (2.15) will also change signs).

Now we assume that the stator inductances in the d - and q -directions (L_d and L_q) are constant and independent of the rotor position². This means that we can write the total flux in the stator as

$$\Psi_{dq0} = \underbrace{\begin{bmatrix} L_d & 0 & 0 \\ 0 & L_q & 0 \\ 0 & 0 & L_0 \end{bmatrix}}_{\mathbf{L}} \begin{bmatrix} i_d \\ i_q \\ i_0 \end{bmatrix} + \Psi_{m,dq0}. \quad (2.12)$$

Using matrix formulation, the phase voltages of the stator can now be written as

$$\underbrace{\begin{bmatrix} v_a \\ v_b \\ v_c \end{bmatrix}}_{\mathbf{v}_{ph}} = \underbrace{\begin{bmatrix} R_s & 0 & 0 \\ 0 & R_s & 0 \\ 0 & 0 & R_s \end{bmatrix}}_{\mathbf{R}_s} \underbrace{\begin{bmatrix} i_a \\ i_b \\ i_c \end{bmatrix}}_{\mathbf{i}_{ph}} + \frac{d}{dt} (\Psi_{ph}). \quad (2.13)$$

Noting that $\Psi_{ph} = \mathbf{T}_{dq,ph}^{-1} \Psi_{dq0}$, we now transform Equation (2.13) to the $dq0$ -coordinates and multiply both sides with $\mathbf{T}_{dq,ph}$, which yields

$$\mathbf{v}_{dq0} = \mathbf{T}_{dq,ph} \mathbf{R}_s \mathbf{T}_{dq,ph}^{-1} \mathbf{i}_{dq0} + \mathbf{T}_{dq,ph} \frac{d}{dt} (\mathbf{T}_{dq,ph}^{-1} \Psi_{dq0}). \quad (2.14)$$

The last term on the right side in Equation (2.14) can, after some tedious manipulation, be expressed as

$$\mathbf{T}_{dq,ph} \frac{d}{dt} (\mathbf{T}_{dq,ph}^{-1} \Psi_{dq0}) = \frac{d}{dt} (\Psi_{dq0}) + \begin{bmatrix} 0 & -\omega_r & 0 \\ \omega_r & 0 & 0 \\ 0 & 0 & 0 \end{bmatrix} \Psi_{dq0} \quad (2.15)$$

where $\omega_r = \frac{d\theta}{dt}$ is the electrical rotor speed. Equation (2.14) can now be written

$$\mathbf{v}_{dq0} = \mathbf{R}_s \mathbf{i}_{dq0} + \mathbf{L} \frac{d}{dt} (\mathbf{i}_{dq0}) + \frac{d}{dt} (\Psi_{m,dq0}) + \begin{bmatrix} 0 & -\omega_r & 0 \\ \omega_r & 0 & 0 \\ 0 & 0 & 0 \end{bmatrix} (\mathbf{L} \mathbf{i}_{dq0} + \Psi_{m,dq0}). \quad (2.16)$$

In component form, Equation (2.16) can be written:

$$\begin{aligned} v_d &= R_s i_d + L_d \frac{di_d}{dt} - \omega_r L_q i_q + \underbrace{(-\psi_{q6} - 6\psi_{d6})}_{\Psi_{d6}} \omega_r \sin(6\theta) + \\ &\quad \underbrace{(-\psi_{q12} - 12\psi_{d12})}_{\Psi_{d12}} \omega_r \sin(12\theta) + \dots, \end{aligned} \quad (2.17)$$

²This is not an obvious assumption, since non-sinusoidal flux distribution also leads to a position dependence of the inductances. These harmonics have often been identified using finite element methods, which is out of the scope for this thesis. Observer-based methods for estimating these harmonics have been developed recently [21] and should be considered in future modelling and control of the machine.

$$v_q = R_s i_q + L_q \frac{di_q}{dt} + \omega_r L_d i_d + \underbrace{(\psi_{d6} + 6\psi_{q6})}_{\Psi_{q6}} \omega_r \cos(6\theta) + \quad (2.18)$$

$$\underbrace{(\psi_{d12} + 12\psi_{q12})}_{\Psi_{q12}} \omega_r \sin(12\theta) + \omega_r \underbrace{\psi_m}_{\Psi_m} + \dots,$$

$$v_0 = R_s i_0 + L_0 \frac{di_0}{dt} - \omega_r \underbrace{3\psi_{03}}_{\Psi_{03}} \sin(3\theta) - \omega_r \underbrace{9\psi_{09}}_{\Psi_{09}} \sin(9\theta) + \dots \quad (2.19)$$

2.2 Mechanical Dynamics

Assuming a stiff rotor shaft, the linearized mechanical dynamics can be expressed as

$$J \frac{d\omega_m}{dt} = T_e - T_l - T_{\text{fric}}. \quad (2.20)$$

Here J is the total moment of inertia of the rotor. T_{fric} is the friction torque and is normally modelled $T_{\text{fric}} = B\omega_m$ where B is known as the *friction coefficient*. ω_m is the mechanical rotor speed, which can be expressed in electrical quantities as $\omega_m = \omega_r/n_p$ where n_p is the *pole pair number*. T_l is the load torque and T_e is the electrical torque, which must be derived.

2.2.1 The Electrical Torque Expression

It is shown in Appendix A that the general expression for electrical power, using matrix formulation, is

$$P_e = \frac{3}{2} (\mathbf{u}_{dq0}^T \mathbf{i}_{dq0}). \quad (2.21)$$

Equations (2.17)–(2.18) can be viewed as a circuit diagram shown in Figure 2.4 where $\mathbf{R}_s = \text{diag}(R_s, R_s, R_s)$, $\mathbf{L} = \text{diag}(L_d, L_q, L_0)$ and \mathbf{E} is the back-emf vector, which can be written as

$$\mathbf{E} = \begin{bmatrix} -\omega_r L_q i_q + \omega_r \Psi_{d6} \sin(6\theta) + \omega_r \Psi_{d12} \sin(12\theta) \\ \omega_r L_d i_d + \omega_r \Psi_{q6} \cos(6\theta) + \omega_r \Psi_{q12} \cos(12\theta) + \omega_r \Psi_m \\ -\omega_r \Psi_{03} \sin(3\theta) - \omega_r \Psi_{09} \sin(9\theta) \end{bmatrix}. \quad (2.22)$$

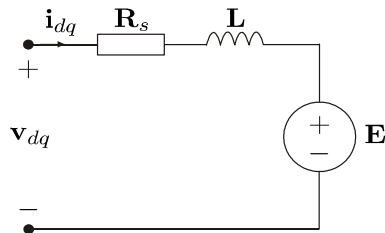


Figure 2.4: Equation (2.17)–(2.18) viewed as a circuit diagram.

In Figure 2.4 we can see that electrical power is dissipated in the resistance matrix and in the back-emf vector. The power produced in the resistances is losses and does not contribute to the electrical torque (it produces only heat). The back-emf vector produces the mechanical torque, which can be calculated using the well-known relation

$$T_e = \frac{P_e}{\omega_m} = \frac{n_p P_e}{\omega_r}. \quad (2.23)$$

Since P_e can be expressed using Equation (2.21), the torque expression becomes

$$\begin{aligned} T_e &= \frac{n_p P_e}{\omega_r} = \frac{3n_p}{2\omega_r} (\mathbf{E}^T \mathbf{i}_{dq0}) \\ &= \frac{3n_p}{2} [\Psi_m i_q + (L_d - L_q) i_d i_q + (\Psi_{d6} \sin(6\theta) + \Psi_{d12} \sin(12\theta)) i_d + \\ &\quad (\Psi_{q6} \cos(6\theta) + \Psi_{q12} \cos(12\theta)) i_q - i_0 (\Psi_{03} \sin(3\theta) + \Psi_{09} \sin(9\theta))]. \end{aligned} \quad (2.24)$$

Now $i_0 = \frac{i_a + i_b + i_c}{3} = 0$ since the machine is wye-connected and the neutral is isolated³. This simplifies the torque expression to

$$\begin{aligned} T_e &= \frac{3n_p}{2} [\Psi_m i_q + (L_d - L_q) i_d i_q + (\Psi_{d6} \sin(6\theta) + \Psi_{d12} \sin(12\theta)) i_d + \\ &\quad (\Psi_{q6} \cos(6\theta) + \Psi_{q12} \cos(12\theta)) i_q]. \end{aligned} \quad (2.25)$$

2.3 Summary of the Transient Model

In summary, the transient model of the permanent magnet synchronous machine with a non-sinusoidal flux distribution can be expressed with the following three equations⁴:

$$v_d = R_s i_d + L_d \frac{di_d}{dt} - \omega_r L_q i_q + \omega_r \Psi_{d6} \sin(6\theta) + \omega_r \Psi_{d12} \sin(12\theta), \quad (2.26)$$

$$v_q = R_s i_q + L_q \frac{di_q}{dt} + \omega_r L_d i_d + \omega_r \Psi_{q6} \cos(6\theta) + \omega_r \Psi_{q12} \cos(12\theta) + \omega_r \Psi_m, \quad (2.27)$$

$$\begin{aligned} J \frac{d\omega_r}{dt} &= \frac{3n_p^2}{2} [\Psi_m i_q + (L_d - L_q) i_d i_q + (\Psi_{d6} \sin(6\theta) + \Psi_{d12} \sin(12\theta)) i_d + \\ &\quad (\Psi_{q6} \cos(6\theta) + \Psi_{q12} \cos(12\theta)) i_q] - n_p T_l - B\omega_r. \end{aligned} \quad (2.28)$$

The difference between the standard model of the PMSM and the above is that the electrical torque is now a function of the rotor position. This leads to torque ripple oscillations which have to be minimized in order to control the machine exactly. All parameters except the amplitude of the flux harmonics (Ψ_{d6} , Ψ_{q6} etc) can be experimentally determined with standard testing procedures (see Part III for the determination of flux harmonics).

³The zero-sequence current can, however, be used to contribute to the torque provided that the machine is not wye-connected, which was pointed out in [3].

⁴The model has the same form as the models stated (not derived) in [3, 22, 27].

2.4 Steady State Model

Since the transient model has now been derived we can easily extract from it a model, valid only for steady state operation. Studying Equations (2.26)–(2.27) we can start with removing the time derivatives since the current is constant in steady state operation. We can also remove harmonics of the back-emf. The coupling $\omega_r L_{d,q}$ can be represented by constant reactances, $\omega_r L_{d,q} \Rightarrow X_{d,q}$ since the speed is constant during steady state operation. Doing this and representing it with *phasors* leads to the following equations:

$$\underline{V}_d = R_s \underline{I}_d - jX_q \underline{I}_q, \quad (2.29)$$

$$\underline{V}_q = R_s \underline{I}_q + jX_d \underline{I}_d + \underline{E}. \quad (2.30)$$

Here \underline{E} represents the fundamental back-emf. Adding these two equations, using $\underline{V}_d + \underline{V}_q = \underline{V}_s$ and $\underline{I}_d + \underline{I}_q = \underline{I}_s$, we find the steady state phasor equation of the salient permanent magnet synchronous motor.

$$\underline{V}_s = R_s \underline{I}_s + jX_d \underline{I}_d - jX_q \underline{I}_q + \underline{E}. \quad (2.31)$$

This equation can also be represented as a phasor diagram, which is shown in Figure 2.5. The angles φ and δ are introduced in the figure. φ is the usual *phase angle*, which relates how much active and reactive power the motor consumes. δ is known as the *power angle* and it relates the active power consumed as well as the stability of the operation point. See [29] for an excellent discussion of steady state behaviour and power angle characteristics of synchronous machines.

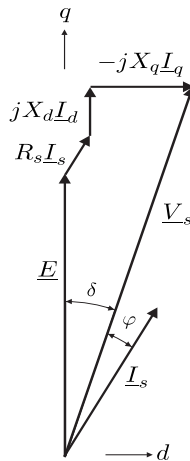


Figure 2.5: The phasor diagram of the steady state model.

Chapter 3

Design of Current Controllers

This section discusses the design of current controllers. The design procedure basically follows the work published by Harnefors et al. [8, 9, 10] but the focus is solely on the present permanent magnet machine for which the transient model was derived in Section 2.

To derive the current controller, we first assume that the current dynamics are much faster than the mechanical dynamics. This means that we can regard ω_r as constant when designing the current controllers. The electrical dynamics are then described by Equations (2.26)–(2.27), which can be represented as a block diagram as shown in Figure 3.1.

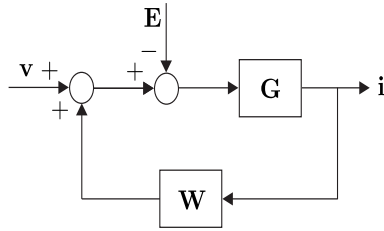


Figure 3.1: Electrical dynamics represented as a block diagram.

Here $\mathbf{v} = [v_d \ v_q]^T$ and $\mathbf{i} = [i_d \ i_q]^T$. \mathbf{E} is the back-emf vector acting as a load disturbance.

$$\mathbf{E} = \begin{bmatrix} \omega_r (\Psi_{d6} \sin(6\theta) + \Psi_{d12} \sin(12\theta)) \\ \omega_r (\Psi_m + \Psi_{q6} \cos(6\theta) + \Psi_{q12} \cos(12\theta)) \end{bmatrix}. \quad (3.1)$$

The transfer function matrix \mathbf{G} consists of two, non-coupled, first order systems which can be written (s denotes the Laplace variable)

$$\mathbf{G} = \begin{bmatrix} \frac{1}{sL_d + R_s} & 0 \\ 0 & \frac{1}{sL_q + R_s} \end{bmatrix}. \quad (3.2)$$

\mathbf{W} represents the coupling of Equations (2.26)–(2.27) and is

$$\mathbf{W} = \begin{bmatrix} 0 & \omega_r L_q \\ -\omega_r L_d & 0 \end{bmatrix}. \quad (3.3)$$

First, we need to decouple the equations. We also add an active damping the purpose of which is to decrease the negative effects of the load disturbance \mathbf{E} . We, therefore, set $\mathbf{v} = \mathbf{v}' - \mathbf{W}\mathbf{i} - \mathbf{R}_a\mathbf{i}$. Here $\mathbf{R}_a = \text{diag}(R_{a,d}, R_{a,q})$ is the active damping (diag denotes the diagonal matrix). With this choice of \mathbf{v} we can draw the block diagram as shown in Figure 3.2 (regarding the selection of active damping, see Section 3.1.1).

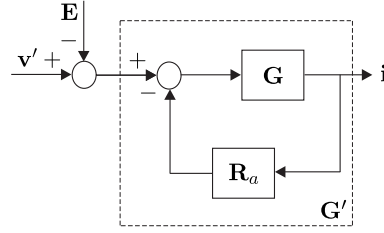


Figure 3.2: The decoupled dynamics.

3.1 Design of Current Controllers Using Internal Model Control

The current controller \mathbf{C} is designed with the *internal model control method* (IMC). IMC is described in detail in [25] but the basic idea of the method is that the feedback is only to contain information about disturbances and model errors. The structure of IMC is shown in Figure 3.3. $\mathbf{G}_{\text{plant}}$ is the actual plant (i. e. the actual machine). In this case, \mathbf{G}' is the first order system shown in Figure 3.2 and the standard choice for selecting \mathbf{C} is then $\mathbf{C} = \mathbf{G}'^{-1}\mathbf{L}$ where $\mathbf{L} = \text{diag}\left(\frac{\alpha_c}{s+\alpha_c}, \frac{\alpha_c}{s+\alpha_c}\right)$ and α_c is a design parameter.

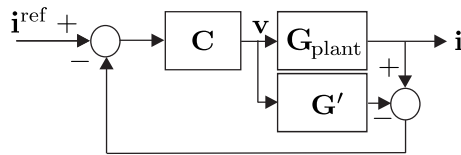


Figure 3.3: IMC structure.

The structure in Figure 3.3 can not, of course, be realized since $\mathbf{G}_{\text{plant}}$ is not exactly known. The IMC structure can, however, be realized as a classical negative feedback structure as shown in Figure 3.4. Studying Figure 3.3, the following relation is easily seen

$$\mathbf{v} = -\mathbf{C}(\mathbf{i} - \mathbf{G}'\mathbf{v}) + \mathbf{C}\mathbf{i}^{\text{ref}}. \quad (3.4)$$

Solving for \mathbf{v} yields

$$\mathbf{v} = (\mathbf{C}^{-1}(\mathbf{I} - \mathbf{C}\mathbf{G}'))^{-1}(\mathbf{i}^{\text{ref}} - \mathbf{i}) \quad (3.5)$$

where \mathbf{I} is the identity matrix. Equation (3.5) can be simplified using ordinary matrix algebra to

$$\mathbf{v} = (\mathbf{I} - \mathbf{C}\mathbf{G}')^{-1} \mathbf{C} (\mathbf{i}^{\text{ref}} - \mathbf{i}). \quad (3.6)$$

Studying Figure 3.4 we see that $\mathbf{v}' = \mathbf{F} (\mathbf{i}^{\text{ref}} - \mathbf{i})$ (ignoring the disturbance \mathbf{E}).

Comparing this with Equation (3.6) we can conclude that the IMC controller \mathbf{C} can be realized as a classical controller \mathbf{F} where

$$\mathbf{F} = (\mathbf{I} - \mathbf{C}\mathbf{G}')^{-1} \mathbf{C} = \alpha_c \begin{bmatrix} L_d + \frac{R_s + R_{a,d}}{s} & 0 \\ 0 & L_q + \frac{R_s + R_{a,q}}{s} \end{bmatrix} = \frac{\alpha_c}{s} \mathbf{G}'^{-1}. \quad (3.7)$$

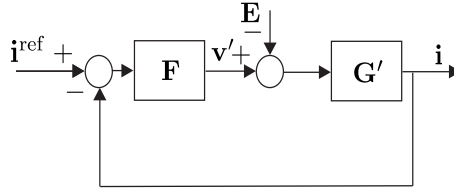


Figure 3.4: Classical control structure.

Equation (3.7) shows that the controller \mathbf{F} consists of two PI-controllers for the d - and q -currents, respectively. The closed loop system \mathbf{G}_{cl} can now be calculated and is

$$\mathbf{G}_{cl} = (\mathbf{I} + \mathbf{G}'\mathbf{F})^{-1} \mathbf{G}'\mathbf{F} = \begin{bmatrix} \frac{\alpha_c}{s + \alpha_c} & 0 \\ 0 & \frac{\alpha_c}{s + \alpha_c} \end{bmatrix}. \quad (3.8)$$

The closed looped system consists of two, stable decoupled first order systems with its poles in $s = -\alpha_c$. From elementary control theory it is known that the rise time, $t_{r,c}$, of a first order system is given by $t_{r,c} = \frac{\ln 9}{\alpha_c}$. This means that the design parameter α_c is determined by the desired rise time. Since the PI-controllers are expressed only in machine parameters and α_c they are now designed.

3.1.1 Selection of Active Damping

We now return to how the active damping is to be chosen to dampen out the load disturbance \mathbf{E} . Figure 3.4 can also be represented with the following equation:

$$\mathbf{i} = \underbrace{(\mathbf{I} + \mathbf{G}'\mathbf{F})^{-1} \mathbf{G}'\mathbf{F}}_{\mathbf{G}_{cl}} \mathbf{i}^{\text{ref}} - \underbrace{(\mathbf{I} + \mathbf{G}'\mathbf{F})^{-1} \mathbf{G}'\mathbf{E}}_{\mathbf{G}_{\text{dist}}}. \quad (3.9)$$

Calculating \mathbf{G}_{dist} yields

$$\mathbf{G}_{\text{dist}} = \begin{bmatrix} \frac{s}{(s + \alpha_c)(sL_d + R_s + R_{a,d})} & 0 \\ 0 & \frac{s}{(s + \alpha_c)(sL_q + R_s + R_{a,q})} \end{bmatrix}. \quad (3.10)$$

We want the disturbances to be damped out as fast as the closed loop, \mathbf{G}_{cl} , so we choose $R_{a,d} = \alpha_c L_d - R_s$ and $R_{a,q} = \alpha_c L_q - R_s$ which yields $\mathbf{G}_{\text{dist}} = \text{diag} \left(\frac{s}{L_d(s + \alpha_c)^2}, \frac{s}{L_q(s + \alpha_c)^2} \right)$. This means that the disturbances have a double pole in $s = -\alpha_c$, which will dampen out the disturbances as fast as \mathbf{G}_{cl} , which has a single pole in $s = -\alpha_c$.

3.1.2 Summary of Current Controller Design

The design of the current controllers using the internal model control method yields two PI-controllers, which are restated here for clarification. $\alpha_c = \ln 9/t_{r,c}$ where $t_{r,c}$ is the desired rise time (in seconds) of a current step response.

$$\begin{aligned} d\text{-axis:} \quad & k_{p,d} = \alpha_c L_d, & k_{i,d} = \alpha_c (R_s + R_{a,d}), & R_{a,d} = \alpha_c L_d - R_s \\ q\text{-axis:} \quad & k_{p,q} = \alpha_c L_q, & k_{i,q} = \alpha_c (R_s + R_{a,q}), & R_{a,q} = \alpha_c L_q - R_s \end{aligned}$$

The current controller designed with IMC has many advantages. It yields very fast step responses without overshoots. It is proven to be stable since the poles of \mathbf{G}_{cl} are real and negative. Its most useful advantage (at least according to the author) is, however, that the controllers are expressed in machine parameters and the desired rise time only. This means that the time consuming design procedure using root locus analysis, Bode plots etc. is avoided.

3.1.3 Torque Ripple Minimization with the IMC Current Controller

To study how the IMC current controller can reduce torque ripple, we start with studying the electrical torque expression, which is restated here for convenience.

$$\begin{aligned} T_e = \frac{3n_p}{2} & [\Psi_m i_q + (L_d - L_q) i_d i_q + (\Psi_{d6} \sin(6\theta) + \Psi_{d12} \sin(12\theta)) i_d + \\ & (\Psi_{q6} \cos(6\theta) + \Psi_{q12} \cos(12\theta)) i_q]. \end{aligned} \quad (3.11)$$

We see that the constant torque term is given by $\Psi_m i_q$ and the reluctance moment $(L_d - L_q) i_d i_q$. A simple, but not the most energy effective [4], method of controlling the torque¹ is to set $i_d^{\text{ref}} = 0$. This does not take advantage of the reluctance moment that the machine can produce due to its saliency. Assuming perfect control of i_d and assuming $\Psi_{q6} \gg \Psi_{q12}$ means that i_q^{ref} is given by

$$i_q^{\text{ref}} = \frac{2T_e^{\text{ref}}}{3n_p (\Psi_m + \Psi_{q6} \cos(6\theta))} \approx \underbrace{\frac{2T_e^{\text{ref}}}{3n_p \Psi_m}}_{i_{q,DC}^{\text{ref}}} - \underbrace{\frac{2T_e^{\text{ref}}}{3n_p \Psi_m^2} \Psi_{q6} \cos(6\theta)}_{i_{q,6}^{\text{ref}}}. \quad (3.12)$$

where the last step is simply a Taylor expansion keeping the first two terms. We see that the reference current in the q -direction contains a constant term $i_{q,DC}^{\text{ref}}$ and a term $i_{q,6}^{\text{ref}}$, varying with six times the rotor speed (assuming $\theta = \omega_r t$). This current reference yields a ripple free torque². Defining $\omega_r' = 6\omega_r$ and assuming $\theta = \omega_r t$ we see that $i_{q,6}^{\text{ref}} \cos(6\theta) = i_{q,6}^{\text{ref}} \cos(\omega_r' t)$. The gain and phase plot of $\mathbf{G}_{cl(2,2)}(j\omega_r')$ is given in Figure 3.5 (note that

¹In [4] the most energy effective (most torque per current rate) current reference is calculated using both a numerical and a simplified on-line torque estimation method. No details of the actual current controller implementation is mentioned, however.

²One of the earliest schemes that proposed this type of current references can be found in [17].

Figure 3.5 is not a Bode plot since the axes are not logarithmic). The rise time is set to $t_{r,c} = 2 \text{ ms} \Rightarrow \alpha_c = \ln 9/t_{r,c} \approx 1098 \text{ s}^{-1}$, which is also used in the implementations.

The base speed of the machine is $\omega_r = 400\pi \text{ rad/s} \Leftrightarrow \omega'_r = 2400\pi \text{ rad/s}$. The phase and amplitude plot show considerable differences between the ideal values (unity gain and no phase shift). For example, the gain is only 0.91 and the phase error -24.5° at $\omega'_r = 500 \text{ rad/s}$. The reason for this is, of course, that $\mathbf{G}_{cl(2,2)}(j\omega'_r)$ is a first order filter, which filters out frequencies above the break frequency α_c . The conclusion that can be drawn is:

Although the IMC current controller can follow constant references very accurately, it cannot control the current to yield a ripple-free torque at higher speeds.

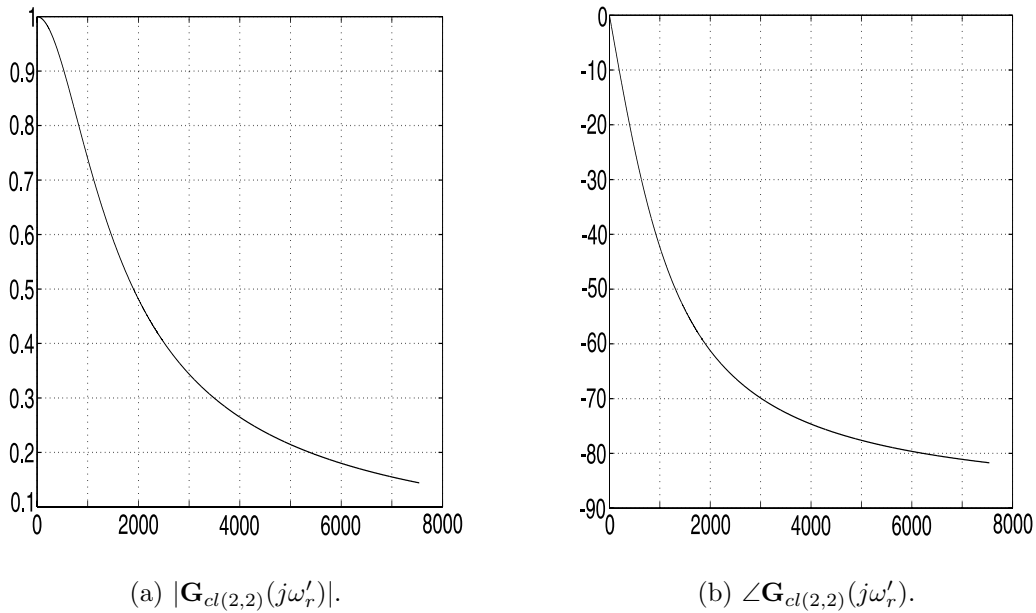


Figure 3.5: Amplitude and phase plot of $\mathbf{G}_{cl(2,2)}(j\omega'_r)$, $0 \leq \omega'_r \leq 2400\pi \text{ rad/s}$.

3.2 A Torque Ripple Minimization Technique Based on Amplitude and Phase Error Estimation

As we have seen, the IMC current controller gives a very rapid step response and has many advantages. Due to the phase and amplitude errors that occur when the controller is trying to follow a varying reference it is not ideal for torque minimization techniques. This section describes a technique to both reduce torque ripples and to keep the IMC current controller. In order to do this, the phase and amplitude errors that occur have to be compensated for.

The first problem that has to be dealt with is how to measure or approximate phase and amplitude errors. Studying Equation (3.12), we can approximate i_q as

$$i_q \approx i_{q,DC}^{\text{ref}} + i_{q,6} \cos(6\theta + \varphi). \quad (3.13)$$

Now we denote the amplitude and phase of the time varying part of Equation (3.13) as $\hat{i}_{q,6}$ and $\hat{\varphi}$. To estimate these phase and amplitude errors we use the MIT rule [35]. The basic idea is to minimize the error e defined as

$$e = i_{q,6} \cos(6\theta + \varphi) - \hat{i}_{q,6} \cos(6\theta + \hat{\varphi}). \quad (3.14)$$

If $e \rightarrow 0$ we know that $\hat{\varphi} = \varphi$ and $\hat{i}_{q,6} = i_{q,6}$. According to the MIT rule, the parameters $\hat{\varphi}$ and $\hat{i}_{q,6}$ are to be updated with the following update rule

$$\frac{d\hat{i}_{q,6}}{dt} = -\gamma_1 e \frac{\partial e}{\partial \hat{i}_{q,6}}, \quad (3.15)$$

$$\frac{d\hat{\varphi}}{dt} = -\gamma_2 e \frac{\partial e}{\partial \hat{\varphi}}. \quad (3.16)$$

where γ_1 and γ_2 are parameters, which set the adaptation rate [35] (see Appendix B). These equations can easily be discretized using forward difference techniques, for example. The basic idea now is that when the phase and amplitude error is approximated with $\hat{\varphi}$ and $\hat{i}_{q,6}$ we simply change the amplitude and phase of the reference value i_q^{ref} .

$$i_q^{\text{ref,shift}} = i_{q,DC}^{\text{ref}} + \frac{i_{q,6}^{\text{ref}}}{\hat{i}_{q,6}} i_{q,6}^{\text{ref}} \cos(6\theta - \hat{\varphi}) \quad (3.17)$$

The control structure is showed in Figure 3.6 where Est and Shift denote the estimator and reference shift, respectively. Studying Figure 3.6 and Equation (3.17) we can see that some problems arise. The first one is that $i_q^{\text{ref,shift}}$ contains $\hat{i}_{q,6}$ in the denominator. This can lead to instabilities for small $\hat{i}_{q,6}$. Another problem is that when $\hat{\varphi}$ is estimated correctly then the reference value will be shifted with $\hat{\varphi}$. This will change the actual current so that it has the correct phase which will lead to $\varphi = 0$. But if $\varphi = 0$, then the reference value will not be shifted. This will lead to oscillations in the phase (the same problem will occur in the amplitude). This means that the shifted reference method, at least in its current form, cannot be used in a closed loop. When the operating point is shifting the phase and amplitude approximation has to be done again and during that time the reference must not be changed.

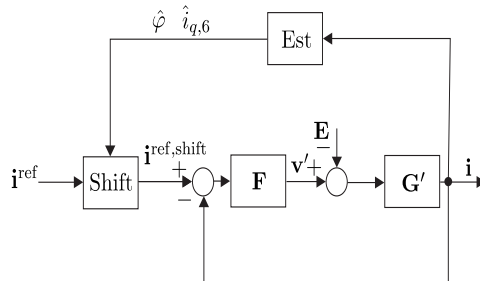


Figure 3.6: Phase and amplitude shift structure.

Figure 3.7-3.8 show simulation results for the proposed method of shifting the reference value. The figures show the maximum steady state torque ripple in percent. The figures

have three graphs comparing the shifted reference method (\diamond), the standard IMC controller not following any varying reference ($*$) and the IMC controller following a varying reference according to Equation (3.12) (\star). The simulations show that the shifted reference method can reduce ripple compared to the standard IMC controller and the IMC controller trying to follow a varying reference. At very slow speeds, the phase and amplitude estimator does not work properly. This is probably due to numerical errors since the forward difference method is used to implement the estimator (Equations (3.15)–(3.16)). Of course, a very good knowledge of the flux harmonics is needed in every operating point to calculate the correct current reference. The flux harmonics are changing in every operating point due to saturation and temperature so a flux linkage observer is needed in order to control the torque accurately.

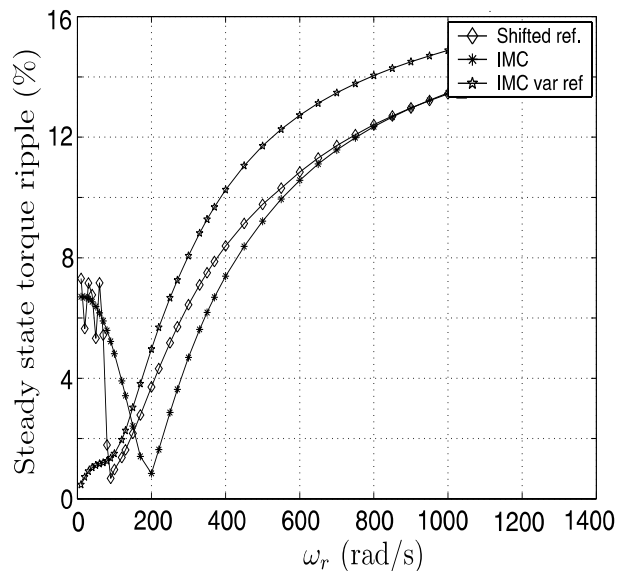


Figure 3.7: Simulated maximum steady state torque ripple at $T_{\text{load}} = 5$ Nm.

Figure 3.7-3.8 also show that the IMC controller following a constant reference reduces the torque ripple compared to the IMC controller following the reference given by Equation (3.12). This is because the active damping cannot dampen out the harmonics in the back-emf completely (cf. Equation (3.9)). This harmonics produce current ripple. At certain operating points this current ripple agrees well with Equation (3.12) and the torque becomes smooth.

To conclude, the shifted reference method requires a very accurate knowledge of the flux linkage harmonics to work properly. To achieve this, a flux linkage observer is needed. The method, in its current form, can only be used in steady state and it does not work properly at low speed due to numerical problems with the implementation of the estimators (Equations (3.15)–(3.16)).

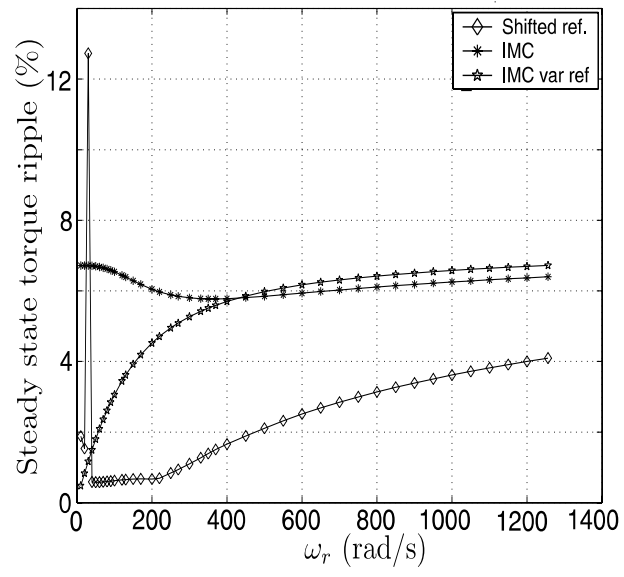


Figure 3.8: Simulated maximum steady state torque ripple at $T_{\text{load}} = 45$ Nm.

Chapter 4

Design of the Speed Controller

This section discusses the design of the speed controller published by Harnefors [11]. The mechanical dynamics are governed by Equation (2.20), which is restated here, expressed in electrical radians

$$\frac{d\omega_r}{dt} = \frac{1}{J} (n_p T_e - n_p T_l - B\omega_r). \quad (4.1)$$

We can still assume that the electrical dynamics are much faster than the mechanical system. This means that with an accurate current controller (like the IMC current controller) we can set $T_e = T_e^{\text{ref}}$ and regard T_e^{ref} as an input signal to Equation (2.20). Treating the load torque as a disturbance (neglecting it) we can design a speed controller with the IMC using the same methods as described in Section 3. The result is

$$k_p = \frac{\alpha_s J}{n_p}, \quad k_i = \frac{\alpha_s B}{n_p}$$

where α_s is the bandwidth of the speed controller ($\alpha_s = \ln 9/t_{r,s}$ where $t_{r,s}$ is the desired rise time of the speed loop). The drawback of the IMC design procedure is that the integration term, k_i , is a function of the friction coefficient B . This is not a good property since the friction coefficient is hard to determine (it varies with speed, temperature, weight on the shaft etc). One solution would be to assume $B = 0$ and perform the IMC design procedure again but the result is simply a P-controller and the integration term is needed to remove remaining errors and to dampen out oscillations.

The proportional term, k_p , is, however, not expressed in B so we keep that term and introduce an *active damping* in T_e^{ref} written as

$$T_e^{\text{ref}} = T_e^{\text{ref}'} - B_a \omega_r. \quad (4.2)$$

Here $B_a \omega_r$ is the active damping term. The transfer function from ω_r to $T_e^{\text{ref}'}$ can be written (s denotes the Laplace variable)

$$G(s) = \frac{\omega_r(s)}{T_e^{\text{ref}'}(s)} = \frac{n_p/J}{s + n_p B_a/J + B/J}. \quad (4.3)$$

To simplify $G(s)$ we set $\alpha_s = n_p B_a/J + B/J$. Solving for B_a yields

$$B_a = \frac{J\alpha_s - B}{n_p} \approx \frac{J\alpha_s}{n_p} \quad (4.4)$$

where the last approximation is valid if $\alpha_s J \gg B$. With this choice of B_a , $G(s)$ is written

$$G(s) = \frac{n_p}{Js + J\alpha_s}. \quad (4.5)$$

Now we can introduce the PI-controller $G_{PI} = k_p e + \frac{k_i}{s} e$ where e is the speed error and k_p is the proportional term given by the IMC design procedure. This means that the closed looped system can be written

$$G_{cl}(s) = \frac{G_{PI}G}{1 + G_{PI}G} = \frac{k_i n_p + J\alpha_s s}{k_i n_p + Js(s + 2\alpha_s)}. \quad (4.6)$$

We want the closed loop system to be of first order, $G_{cl}(s) = \frac{\alpha_s}{s + \alpha_s}$. With this choice of G_{cl} , solving Equation (4.6) for k_i yields $k_i = J\alpha_s^2/n_p$.

4.1 Summary of Speed Controller Design

The design of the speed controller uses internal model control to design the proportional term of the PI controller, treating the load torque as a disturbance. The integration term is calculated with the help of an active damping and with a desire for a closed loop of the first order. The controller is restated here for clarification. $\alpha_s = \frac{\ln 9}{t_{r,s}}$ where $t_{r,s}$ is the desired rise time of the speed loop. Since the speed loop is added as an outer loop to the current loop it is suggested that α_s is chosen at least a decade slower than α_c .

$$\begin{aligned} \text{PI-controller:} \quad & k_p = \frac{\alpha_s J}{n_p}, \quad k_i = J\alpha_s^2/n_p \\ \text{Active damping:} \quad & T_e^{\text{ref}} = T_e^{\text{ref}'} - B_a, \quad B_a = \frac{J\alpha_s}{n_p} \end{aligned}$$

Chapter 5

Sensorless Control of the Machine using Saliency

This section describes a method to estimate the rotor position and the rotor speed based on the injection of high frequency voltages. The method presented here is based on the work by Corley and Lorenz [5] together with the position and speed estimator proposed by Harnefors and Nee [7].

The basic idea is to inject a high frequency voltage in the *assumed* d -direction. From the current in the assumed q -direction the actual rotor position can be extracted. The actual and assumed rotor position (d -direction) is shown in Figure 5.1 where hats ($\hat{}$) denote an estimated parameter.

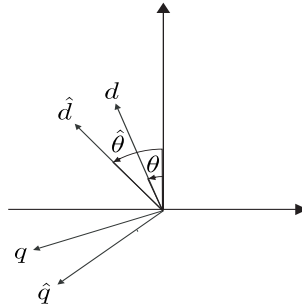


Figure 5.1: Actual dq -coordinates and estimation ($\hat{d}\hat{q}$).

From Figure 5.1 we can calculate the voltages in the d - and q -directions from the injected voltages in the \hat{d} - and \hat{q} -directions.

$$v_d = v_{\hat{d}} \cos(\hat{\theta} - \theta) - v_{\hat{q}} \sin(\hat{\theta} - \theta) \quad (5.1)$$

$$v_q = v_{\hat{d}} \sin(\hat{\theta} - \theta) + v_{\hat{q}} \cos(\hat{\theta} - \theta) \quad (5.2)$$

If we now define the angular error, $\tilde{\theta}$, as $\tilde{\theta} = \theta - \hat{\theta}$ we can write Equations (5.1)–(5.2) in matrix form:

$$\mathbf{v} = \underbrace{\begin{bmatrix} \cos \tilde{\theta} & \sin \tilde{\theta} \\ -\sin \tilde{\theta} & \cos \tilde{\theta} \end{bmatrix}}_{\mathbf{T}} \hat{\mathbf{v}}. \quad (5.3)$$

The inverse is $\hat{\mathbf{v}} = \mathbf{T}^{-1}\mathbf{v}$. Now a high frequency voltage is injected in the \hat{d} -direction,

$$\hat{\mathbf{v}} = \begin{bmatrix} V \cos \omega_e t \\ 0 \end{bmatrix}. \quad (5.4)$$

Here $\omega_e \gg \omega_r$. Now we want to compute the currents that this voltage produces. At standstill $\omega_r = 0$ rad/s. Assuming that $\{\omega_e L_d, \omega_e L_q\} \gg R_s$ we can reduce Equations (2.26)–(2.27) to

$$\mathbf{v} = \mathbf{L} \frac{d}{dt} \mathbf{i}. \quad (5.5)$$

Here $\mathbf{v} = [v_d \ v_q]^T$, $\mathbf{i} = [i_d \ i_q]^T$ and $\mathbf{L} = \begin{bmatrix} L_d & 0 \\ 0 & L_q \end{bmatrix}$. To calculate the current we simply integrate Equation (5.4):

$$\mathbf{i} = \mathbf{L}^{-1} \int_0^t \mathbf{v} dt. \quad (5.6)$$

Since the actual rotor position is not known we transform Equation (5.4) to the estimated coordinates using Equation (5.3).

$$\hat{\mathbf{i}} = \mathbf{T}^{-1} \mathbf{L}^{-1} \int_0^t \mathbf{T} \hat{\mathbf{v}} dt. \quad (5.7)$$

If $\tilde{\theta}$ is changing slowly compared with the high frequency signal ($\cos \omega_e t$) we can regard \mathbf{T} as constant and move it out from the integration sign.

$$\hat{\mathbf{i}} = \mathbf{T}^{-1} \mathbf{L}^{-1} \mathbf{T} \int_0^t \hat{\mathbf{v}} dt. \quad (5.8)$$

Computing the product $\mathbf{T}^{-1} \mathbf{L}^{-1} \mathbf{T}$ yields

$$\hat{\mathbf{i}} = \mathbf{T}^{-1} \mathbf{L}^{-1} \mathbf{T} \int_0^t \hat{\mathbf{v}} dt = \left(\frac{L_q + L_d}{2L_q L_d} \mathbf{I} + \frac{L_q - L_d}{2L_q L_d} \begin{bmatrix} \cos 2\tilde{\theta} & \sin 2\tilde{\theta} \\ \sin 2\tilde{\theta} & -\cos 2\tilde{\theta} \end{bmatrix} \right) \int_0^t \hat{\mathbf{v}} dt. \quad (5.9)$$

The current in the \hat{d} - and \hat{q} -directions can now be calculated and is

$$i_{\hat{d}} = \frac{L_q + L_d}{2L_q L_d} \frac{V}{\omega_e} \sin \omega_e t + \frac{L_q - L_d}{2L_d L_q} \frac{V}{\omega_e} \sin \omega_e t \cos 2\tilde{\theta}, \quad (5.10)$$

$$i_{\hat{q}} = \frac{L_q - L_d}{2L_d L_q} \frac{V}{\omega_e} \sin \omega_e t \sin 2\tilde{\theta}. \quad (5.11)$$

Multiplying $i_{\hat{q}}$ by $\sin \omega_e t$ and filtering out the constant term with a low-pass filter (LPF) yields

$$\varepsilon = \text{LPF}\{i_{\hat{q}} \sin \omega_e t\} = \frac{L_q - L_d}{4L_q L_d} \frac{V}{\omega_e} \sin 2\tilde{\theta}. \quad (5.12)$$

We can see that ε is zero if $L_d = L_q$, which is the case for non-salient machines. This means that the method cannot be applied on this type of machine. Using Equation (5.12) and solving for θ yields

$$\theta = \hat{\theta} + \frac{1}{2} \arcsin \left(\frac{4L_d L_q \omega_e \varepsilon}{V(L_q - L_d)} \right) - n\pi, \quad n = 0, \pm 1, \pm 2, \dots \quad (5.13)$$

Equation (5.13) shows that this method yields an uncertainty of π electrical radians. This uncertainty can be removed if the machine is properly lined up ($\theta \approx 0$ rad) before starting or using some suitable initiation process.

5.1 A Non linear Observer for Estimation of Rotor Angle and Rotor Speed

The injection of a high frequency voltage, as described in the previous section, leads to an error signal, ε . To estimate the rotor position and speed some kind of observer has to be applied to make sure that the estimated values converge to the actual ones. This section describes the non linear observer proposed by Harnefors.

The observer is written in state space form, which is implemented using the forward difference approximation.

$$\hat{\omega}_r = \gamma_1 \varepsilon, \quad (5.14)$$

$$\hat{\theta} = \hat{\omega}_r + \gamma_2 \varepsilon. \quad (5.15)$$

γ_1 and γ_2 are constants and should be chosen as

$$\gamma_1 = \frac{2\rho^2 \omega_e L_d L_q}{V(L_q - L_d)}, \quad (5.16)$$

$$\gamma_2 = \frac{4\rho \omega_e L_d L_q}{V(L_q - L_d)}. \quad (5.17)$$

The poles of the linearized observer are then placed in $-\rho$ and should be selected as

$$\rho = \sqrt{\frac{\alpha_s \Delta \omega_{\text{ref}}}{\sin 2\tilde{\theta}_{\text{max}}}} \quad (5.18)$$

where α_s is the bandwidth of the speed loop. $\Delta \omega_{\text{ref}}$ is the maximum change of the speed reference (assuming that it changes in steps) and $\tilde{\theta}_{\text{max}}$ is the maximum allowed position estimation error.

Part III

Implementations

Chapter 6

Measurement of Flux Linkage Harmonics

It is possible to measure the flux harmonics Ψ_{d6} , Ψ_{d2} , etc. by measuring the open-circuit phase voltages at constant speed, transforming the voltages to the dq -coordinates and then perform a frequency analysis using the Fast Fourier Transform (FFT). The transformation to the dq -coordinates requires an accurate value of the electrical angle θ . The rotor position angle can be approximated from the measured rotor speed or the period of the measured voltage (see below). Another method is to study Equation (2.11) and (2.17)–(2.18). We see that the flux harmonics can be expressed as

$$\Psi_{d6} = -\psi_{q6} - 6\psi_{d6} = -(-\psi_5 + \psi_7) - 6(\psi_5 + \psi_7) = -5\psi_5 - 7\psi_7, \quad (6.1)$$

$$\Psi_{d12} = -\psi_{q12} - 12\psi_{d12} = -(-\psi_{11} + \psi_{13}) - 12(\psi_{11} + \psi_{13}) = -11\psi_{11} - 13\psi_{13}, \quad (6.2)$$

$$\Psi_{q6} = \psi_{d6} + 6\psi_{q6} = \psi_5 + \psi_7 + 6(-\psi_5 + \psi_7) = -5\psi_5 + 7\psi_7, \quad (6.3)$$

$$\Psi_{q12} = \psi_{d12} + 12\psi_{q12} = \psi_{11} + \psi_{13} + 12(-\psi_{11} + \psi_{13}) = -11\psi_{11} + 13\psi_{13}. \quad (6.4)$$

The open-circuit phase voltage v_a during constant speed ($\theta = \omega_r t$) can be expressed as

$$v_a = \frac{d\Psi_{m,a}}{dt} = -\psi_1\omega_r \sin(\omega_r t) - 3\psi_3\omega_r \sin(3\omega_r t) - 5\psi_5\omega_r \sin(5\omega_r t) + \dots \quad (6.5)$$

Since $v_b = \frac{d\Psi_{m,a}(\omega_r t - 2\pi/3)}{dt}$ and $v_c = \frac{d\Psi_{m,a}(\omega_r t + 2\pi/3)}{dt}$ it is easy to show that $v_a + v_b + v_c = 0$ (at least in the ideal, open-circuit case). Equation (6.5) shows that flux harmonics can be found by performing a frequency analysis on $-v_a$. The angular speed, ω_r , can be extracted from the period time, T , since $\omega_r = \frac{2\pi}{T}$, so no angular position is needed to determine the harmonics. We see that ψ_1 is found at the frequency ω_r and $3\psi_3$ is found at the frequency $3\omega_r$, and so on. To measure the phase voltage v_a we can either measure the line-to-neutral voltage or, if the neutral point is unavailable, measure two line voltages¹ as

$$(v_a - v_b) - (v_c - v_a) = v_a - v_b - v_c + v_a = 3v_a. \quad (6.6)$$

Figure 6.1(a) shows v_a at $\omega_r = 130$ rad/s. The sampling frequency is 5 kHz and the signal is not filtered. The small ripple on the signal is due to the interaction between the stator

¹The author wishes to thank Mr. Vladan Petrovic [27] for tips on measuring two line voltages if the neutral point is unavailable.

slots and the rotor. The frequency of this ripple is 21 times the fundamental, which can be seen in Figure 6.1(b). Note that the fundamental is much bigger than the harmonics (the top of the fundamental is not shown) and Figure 6.1(b) only shows a zoom of the harmonics.

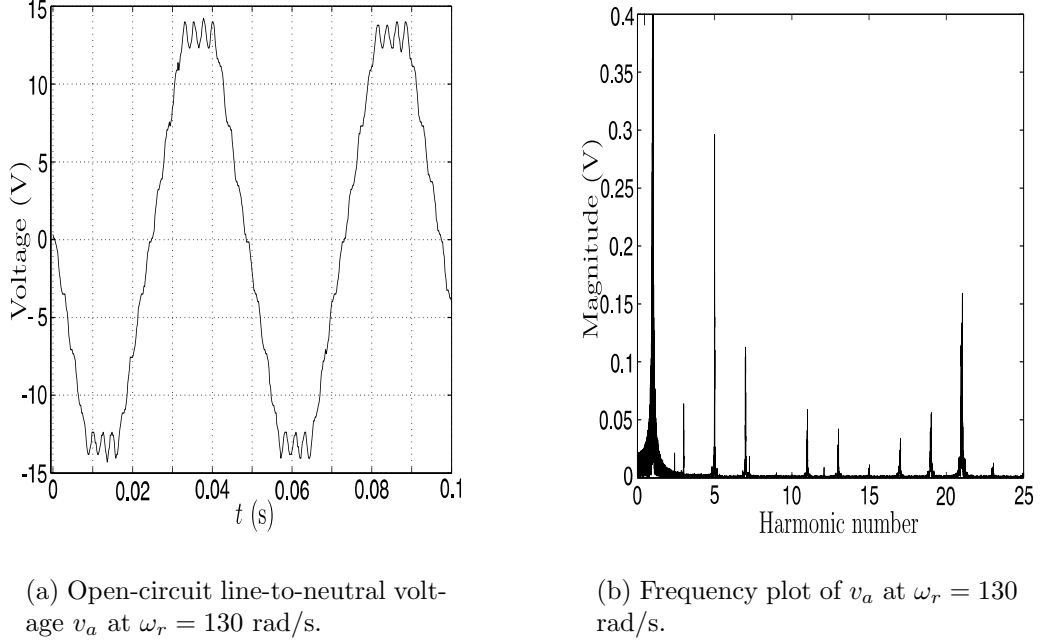
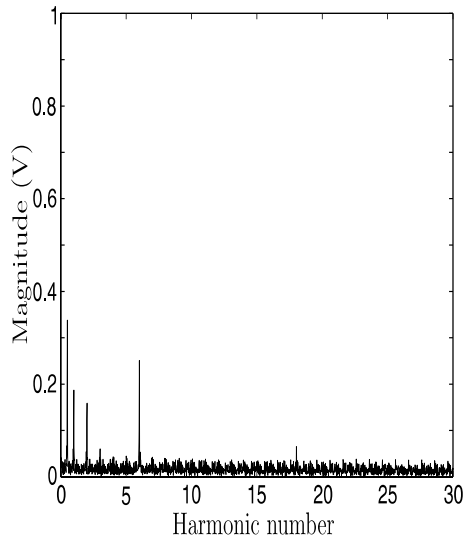


Figure 6.1: Measurement of the open-circuit voltage, v_a .

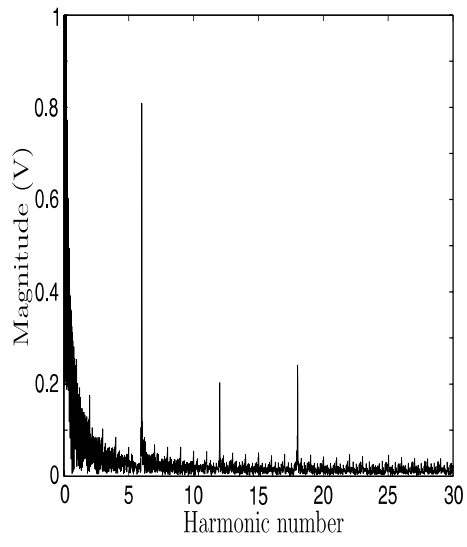
With the measurement system used it was easy to measure both the rotor position and the three phase voltages. The dq -transformation was done in Matlab and Figure 6 shows frequency plots of v_d and v_q (note that the peak of the fundamental in v_q is not shown). The expected harmonics are multiples of 6 and this is clearly seen in both v_d and v_q . The measurement showed that harmonics of order 12 are small compared to harmonics of order 18. v_d also has harmonics of order 0.5, 1 and 2. These harmonics are probably due to asymmetries in the stator/rotor design and were neglected. The most significant harmonic is Ψ_{q6} which is approximately 6% the size of Ψ_m . The result of the measurements is shown in Table 6.1.

Ψ_m	103.91 mWb
Ψ_{d6}	2.30 mWb
Ψ_{d12}	0.26 mWb
Ψ_{d18}	0.57 mWb
Ψ_{q6}	6.22 mWb
Ψ_{q12}	1.60 mWb
Ψ_{q18}	2.04 mWb

Table 6.1: Measured flux harmonics in the dq -coordinates.



(a) v_d .



(b) v_q .

Figure 6.2: Frequency plot of v_d and v_q and $\omega_r = 130$ rad/s.

Chapter 7

Implementation of the Current Controller

The current controller described in Section 3 is easily implemented. The controller algorithm is written in C-code, which is compiled to machine code suitable for the DSP-system (information about the DSP-system can be found in Appendix C). In order to avoid integration windup in the overmodulation range, a back-calculation algorithm [8] is used. The rotor speed is calculated from the rotor position given by the resolver using a backward Euler differentiation and a first order Butterworth low pass filter to reduce the noise in the differentiation process [20].

7.1 Step in i_q

The voltage source inverter (VSI) is fed by a DC voltage, u_{dc} , which was set to 100 V. In the first measurement the current references were set $i_d^{\text{ref}} = 0$ A and $i_q^{\text{ref}} = \pm 15$ A. The sign of i_q^{ref} (and the sign of the electrical torque) is changed to keep $-50 \leq \omega_r \leq 50$ rad/s. The rise time, $t_{r,c}$, is set at 2 ms. The permanent magnet machine is connected, through a gearbox, to a DC machine. No load torque is applied to the shaft.

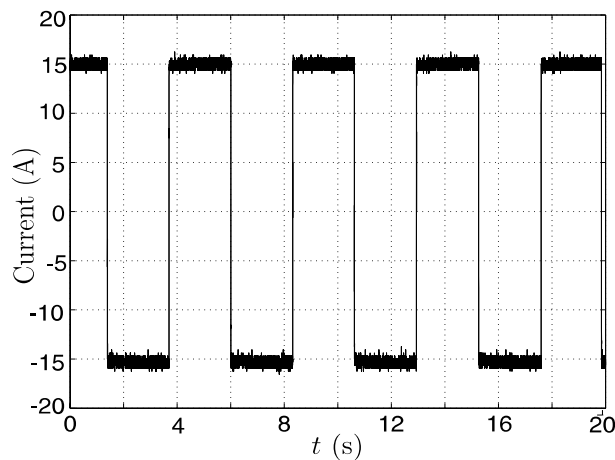


Figure 7.1: Current in q -direction during step changes in the reference value.

Figure 7.1 shows the measured i_q . Figure 7.2 shows a zoom of the step response. We can see that the response contains no overshoots and that the desired value of i_q has been reached. Studying the measurements further, the rise time of the current step is approximately 2.5 ms, which corresponds well to the desired rise time (2 ms).

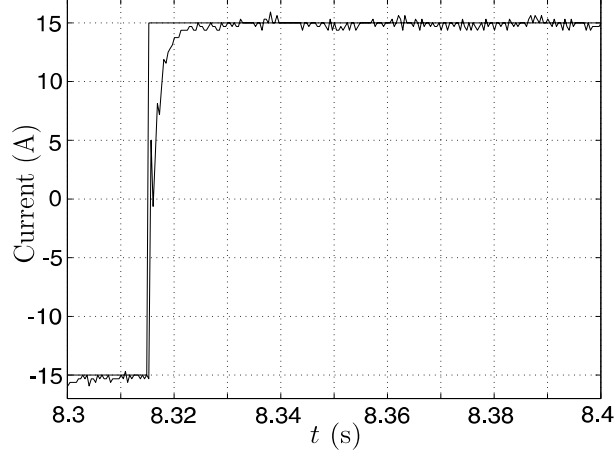


Figure 7.2: Zoom in of the measured step response of i_q .

7.1.1 Approximation of Moment of Inertia and Friction Torque

Since the implemented current controller is very fast and accurate it makes it possible to approximate the moment of inertia of the shaft, J , and the friction torque, T_{fric} , which are not known. Rotor speed variations during the measurements are shown in Figure 7.3. Since the currents are known we can calculate the electrical torque using Equation (3.11) and neglect the ripple terms. The rotor speed changes almost linearly, which implies constant acceleration but the acceleration depends on the sign of ω_r . This implies that friction torque can be modelled as a constant term only depending on the sign of ω_r .

$$T_{\text{fric}} = B_{\text{fric}} \cdot \frac{\omega_r}{|\omega_r|} = B_{\text{fric}} \cdot \text{sign}(\omega_r), \quad -50 \leq \omega_r \leq 50 \text{ rad/s} \quad (7.1)$$

Naturally, this assumption is only valid in the measured speed range ($-50 \leq \omega_r \leq 50$ rad/s). The two different slopes, which are calculated using a first order polynomial fit, of w_r , gives us two equations which make it possible to solve for both J and T_{fric} . The result is

$$J = 168.9 \cdot 10^{-3} \text{ kgm}^2,$$

$$B_{\text{fric}} = 2.36 \text{ kgm}^2/\text{s}.$$

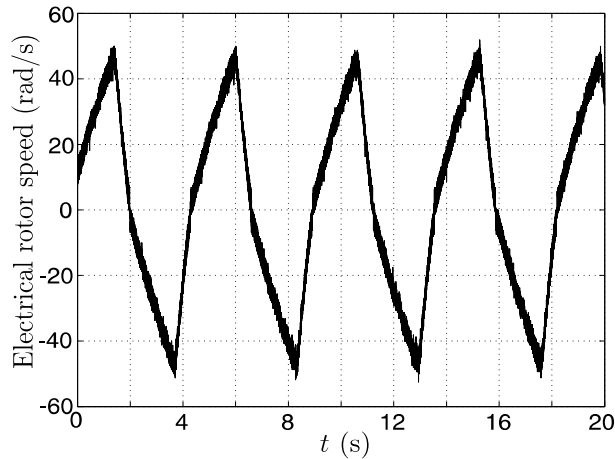


Figure 7.3: The electrical rotor speed, ω_r , during the current step measurement.

7.1.2 Simulation of the Machine

Since all parameters of the system are known, it is possible to simulate the machine using Equations (2.26)–(2.28). The step response is shown in Figure 7.4 where the both the measured (boxes) and simulated (circles) responses are shown. A 10% error is added to each parameter in the simulation. The period and appearance of the simulated speed pulsation (from -50 rad/s to 50 rad/s) was approximately the same as the period of the measured speed pulsation. This shows that the approximations of J and B_{fric} are acceptable.

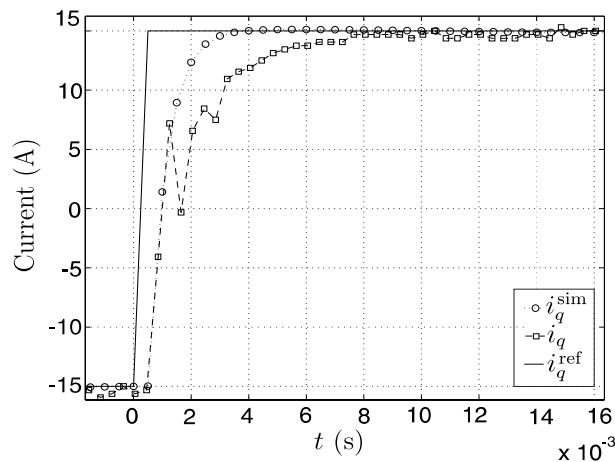


Figure 7.4: Measured and simulated step response of i_q .

The simulations show a very small ripple in i_q due to the harmonics in the back-emf, which are handled as a disturbance in the control system (cf. Figure 3.1). The ripple is small because the speed is so low, $\omega_r \leq 50$ rad/s $\Rightarrow \omega'_r \leq 300$ rad/s (compare with figure 3.5). This frequency is low so the current controller can remove the disturbance.

7.2 Implementation of the Sensorless Algorithm

A few parameters have to be set correct in order to get the sensorless algorithm to work properly (see Chapter 5). The amplitude and frequency of the injected high frequency voltage was set to $V = 7$ V and $f_e = 400$ Hz. The poles of the linearized observer were set so $\rho \approx 42$. In order to get the system to work properly the bandwidth of the current controller was set to $\alpha_c \approx 183$ (the rise time of the current controller was lowered from 2 ms to 12 ms). The low pass filter was a first order Butterworth filter with a break frequency of 80 Hz designed with the Signal Processing toolbox in Matlab.

7.2.1 Step in i_q

In order to see if the sensorless algorithm worked properly, it was tested with the same procedure as in Section 7.1. This means that the current reference in the q -direction changed stepwise, $i_q^{\text{ref}} = \pm 15$ A and the d -reference current was set to $i_d^{\text{ref}} = 0$ A. The results of the measurements are shown in Figure 7.5–7.9.

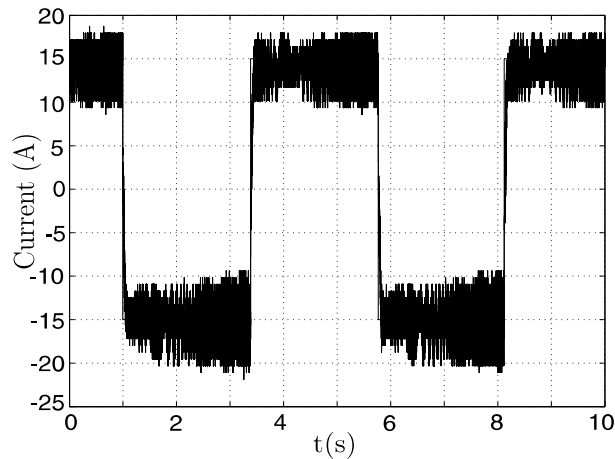


Figure 7.5: Measured i_q and i_q^{ref} .

Figure 7.5 shows the actual current in the q -direction. Comparing this with Figure 7.1, we can see that the current contains more ripple but the current controller is working properly. Due to the injected high frequency voltage in the d -direction, the d -current oscillates at 400 Hz and this ripple is clearly seen in Figure 7.6 (note the different time scales).

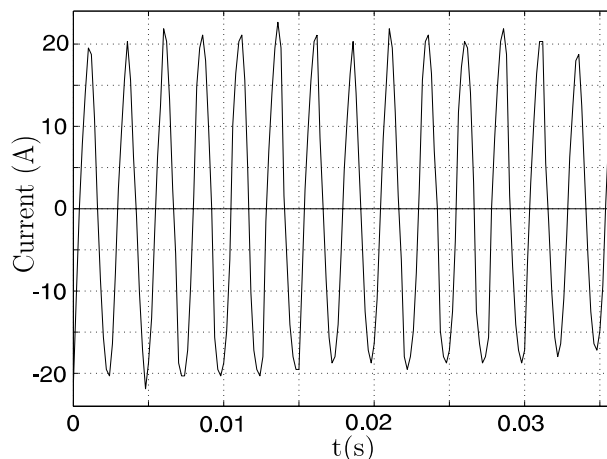


Figure 7.6: Measured i_d and $i_d^{\text{ref}} = 0$.

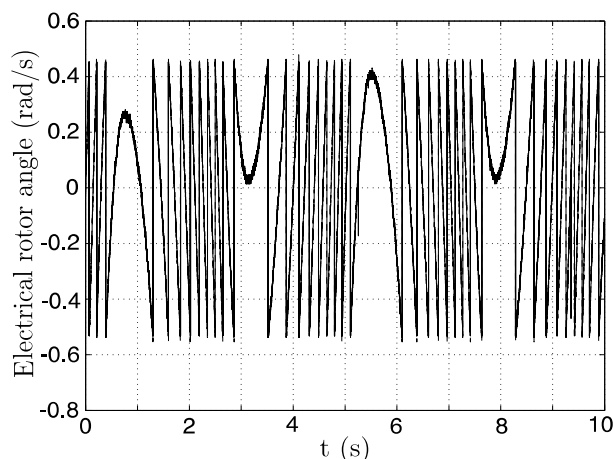


Figure 7.7: Measured rotor angle, θ and estimated rotor angle $\hat{\theta}$.

Figures 7.7–7.9 show the measured and estimated rotor position and rotor speed. We can see that the estimated values are very close to the measured ones. Figure 7.8 shows the estimated rotor error, $\tilde{\theta}$ and $\tilde{\theta} \leq 0.06$ rad. When the rotor position passes zero it changes stepwise from 2π to zero and this causes $\tilde{\theta}$ to be very big during one or two samples. This is shown as the small spikes in $\tilde{\theta}$. Since the estimation works properly, $\tilde{\theta} \approx 0$ rad and Equation (5.10) can be approximated as

$$i_d \approx \frac{V}{L_d \omega_e} \sin \omega_e t \approx 14 \sin(\omega_e t).$$

This is one of the drawbacks of this type of sensorless algorithm. Since $v_d = V \sin \omega_e t$ this means that the instantaneous power varies as $p(t) = v_d(t)i_d(t) = \frac{V^2 \sin(2\omega_e t)}{L_d \omega_e}$. This power flows between the DC-link and the machine and increases system losses.

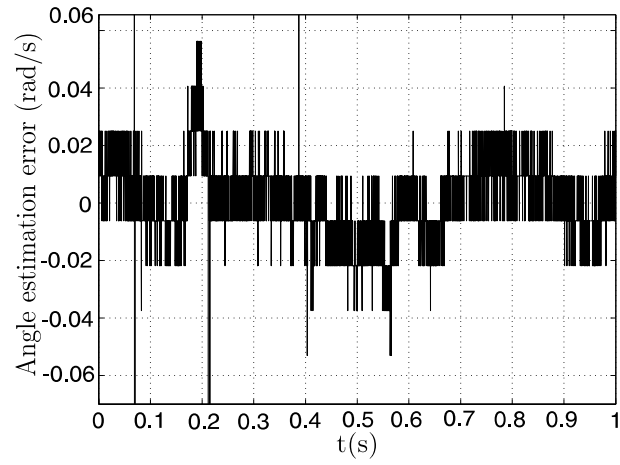


Figure 7.8: Rotor angle estimation error, $\tilde{\theta}$.

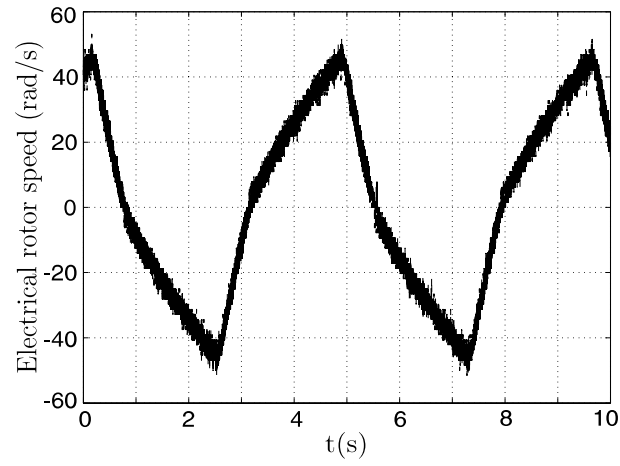


Figure 7.9: Measured rotor speed, ω_r and estimated speed $\hat{\omega}_r$.

Chapter 8

Measurement of Torque and Current Ripple

To verify if the model derived in Part II is valid, the torque and current of two different operation points were measured and compared with simulations. The current was measured with the built in LEM modules in the VSI and transformed, online to the rotor fixed dq -coordinates using the resolver signal. The torque was measured with a torque transducer mounted on the shaft of the machine. See Appendix D for pictures of the measurement setup and [20] for a complete description of the laboratory setup.

8.1 No Load Measurement

In the first measurement, no load is applied to the shaft and the load torque consists only of the friction torque. Figure 8.1 shows the measured and simulated currents, in d - and q -direction, during one electrical period. The measured rotor speed is $\omega_r = 160.7$ rad/s which is slow since the base speed is $\omega_{\text{base}} = 1257$ rad/s. The dashed graphs are simulated currents. The upper graphs in the figure show the measured and simulated currents. In the lower graphs the measured current is filtered using a fifth order Butterworth low pass filter with a break frequency at $\omega_{\text{break}} = 40\omega_r$. The break frequency was chosen to filter disturbances in the small load measurement (see Section 8.2). The current references are set to $i_d^{\text{ref}} = 0$ A and $i_q^{\text{ref}} = 12.7$ A. The current ripple is due to harmonics in the back-emf (cf. Equation (3.9)).

Figure 8.2 shows the measured (upper graph) and simulated (lower graph) torque spectra. The peaks at $6\omega_r$, $12\omega_r$ and $18\omega_r$ are clearly seen in both simulations and measurements. This is also due to the harmonics in the back-emf (cf. Equations (2.24)–(2.25)). The measured values also show a large peak at $11.5\omega_r$ but this peak is speed dependent and is specific of this operating point. This peak could be produced by the pulse-width-modulation (PWM) pattern produced by the VSI or by mechanical oscillations. Limitations of the derived model, the accuracy of the used spectral analysis and the bandwidth of the torque transducer are three sources of error, since the amplitude of the measured and simulated torque peaks are not corresponding exactly.

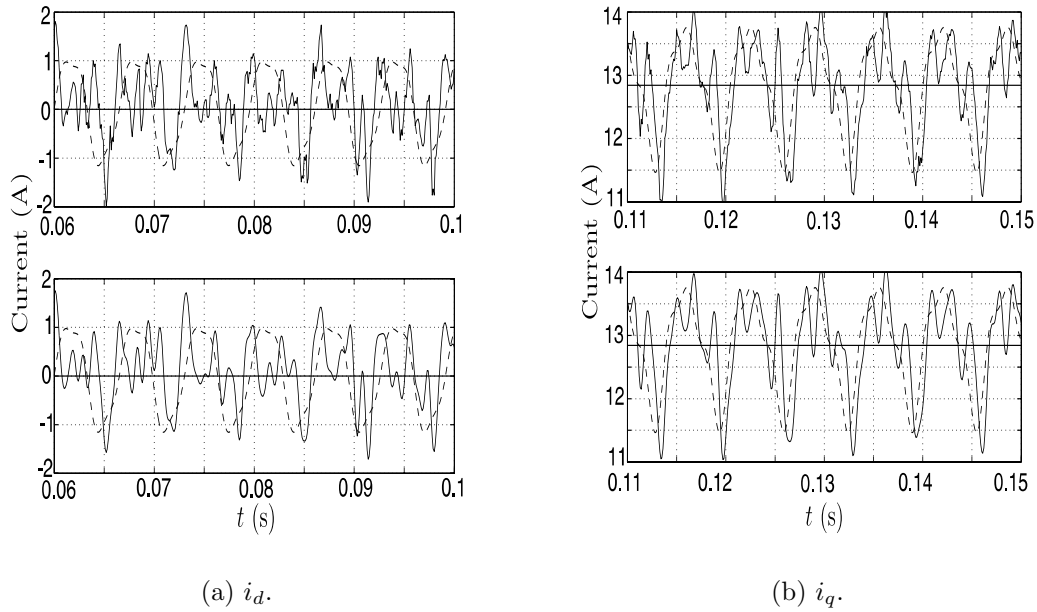


Figure 8.1: No load currents, i_q and i_d , during one electrical period. Dashed graphs are simulated results.

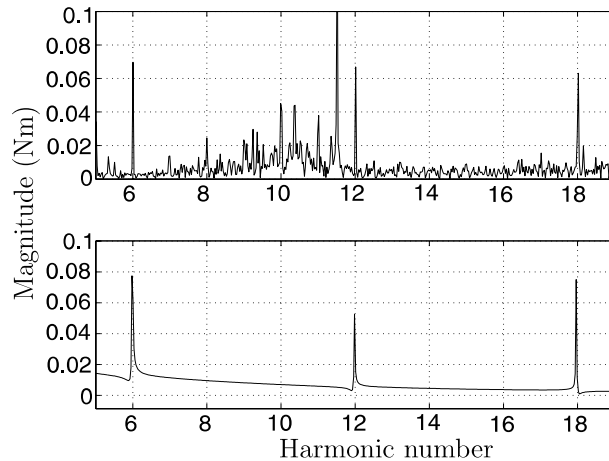


Figure 8.2: Measured (upper) and simulated (lower) no load torque.

8.2 Small Load Measurement

In this measurement, the DC machine controls the speed of the PMSM. The DC machine is controlled with a thyristor converter and a large inductance (20 mH) is connected between the thyristor converter and the DC machine to smoothen out the DC-current. The speed is held at $\omega_r = 62$ rad/s, torque producing currents are injected in the PMSM and the torque and current is measured. The current references are set to $i_d^{\text{ref}} = 0$ A and $i_q^{\text{ref}} = 5.7$ A

Figure 8.3 shows the measured and simulated currents during one electrical period. The upper graphs show the actual, non filtered currents (and simulations). In the lower

graphs the measured currents are filtered using the same filter as in Section 8.1. The measured currents are much more distorted during load but the filtered currents agree roughly with the simulations (dashed).

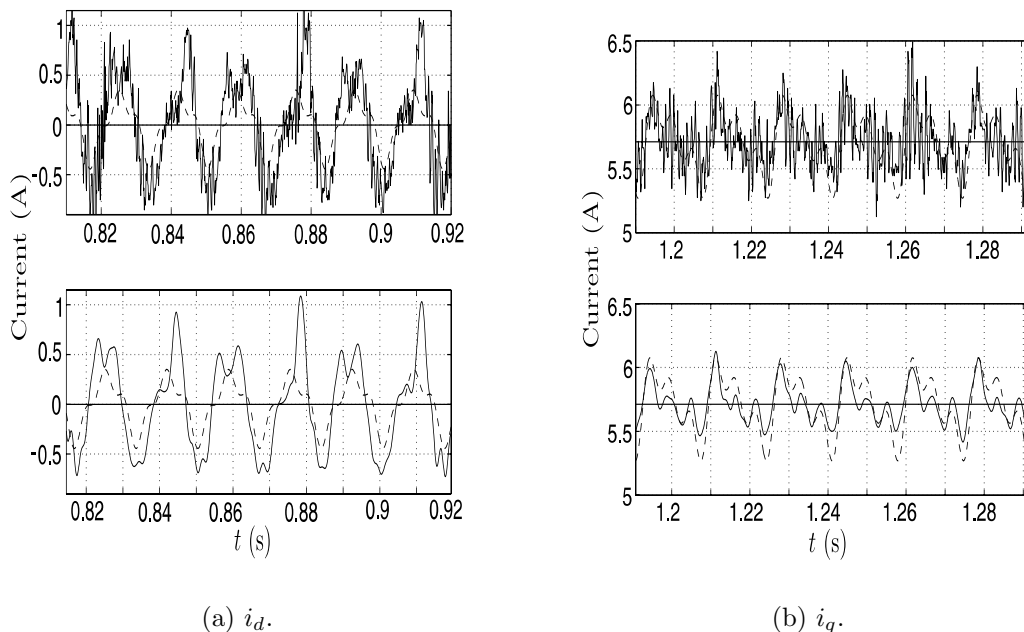


Figure 8.3: Small load currents, i_d and i_q , during one electrical period. Dashed graphs are simulated results.

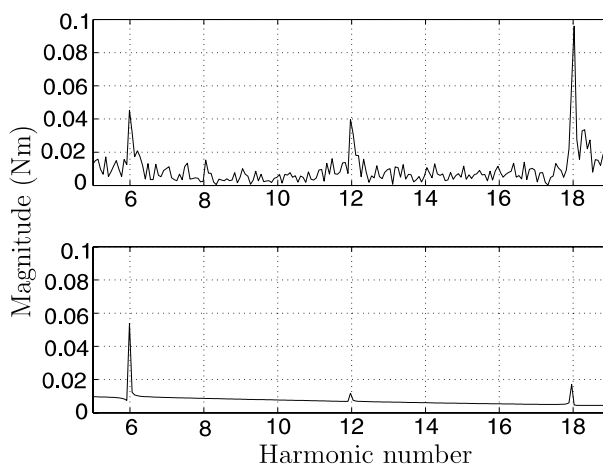


Figure 8.4: Measured (upper) and simulated (lower) small load torque.

The measured and simulated torque spectra do not agree well in amplitude sense but the peaks at $6\omega_r$, $12\omega_r$ and $18\omega_r$ are clearly seen. Figure 8.5 shows the total measured torque spectra and it can be seen that the ripple also consists of low order harmonics ($0.5\omega_r$, $1\omega_r$, $2\omega_r$ etc.). A large peak of order $24\omega_r$ is also shown. This peak is due to the cogging torque produced by the machine. The order of the cogging torque is the number of stator slots divided by the pole pair number. The machine has 48 stator slots and the

pole pair number is 2. Since the the load of the machine is so small the cogging torque is the dominant ripple harmonic in this measurement.

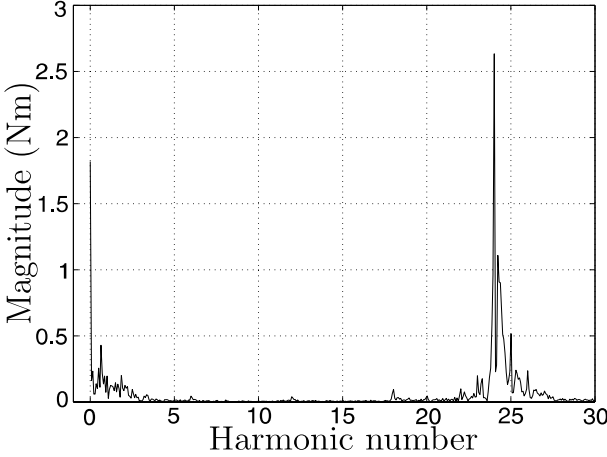


Figure 8.5: Cogging torque (24th harmonic).

Chapter 9

Conclusions

This thesis has discussed different aspects of control of permanent magnet synchronous machines. The effects of the non-sinusoidal flux linkage was included in the transient model of the machine. The flux linkage harmonics were measured from an open-circuit voltage measurement. The predicted current and torque ripple harmonics are multiples of 6 and this was shown in the measurements. The torque ripple produced by the cogging torque and the flux linkage harmonics is not believed to be a problem in HEV applications, due to the large moment of inertia of a car which will dampen out ripple very efficiently.

The method to reduce torque ripples using shifted references requires very accurate knowledge of the flux linkage harmonics and cannot, in its current form, be implemented in a closed loop. If these problems are solved the method may be of use.

The described current controller, based on internal model control, was implemented with good results. The predicted current step responses agreed well with the measurements and no overshoots were observed. Since the current controller followed the current references accurately, it was possible to approximate the moment of inertia of the shaft and the constant friction torque at low speeds. Due to the harmonics in the back-emf the current contains small oscillations which could not be damped out entirely by the chosen active damping.

The saliency of the machine made it possible to control the machine, without a rotor position sensor, using high frequency signal injection. This was also implemented in the laboratory and tested, with good results, at low speeds, with no load.

9.1 Further Work

Regarding the flux linkage harmonics, more detailed open-circuit voltage measurements should be carried out in the whole speed range for a more complete determination of them. The back-emf during operation can also be determined using different kind of observers [27, 13]. Implementing a fully functioning back-emf observer is of importance since it should make it easier to analyze the large current ripple at high loads, reported in [20]. A flux linkage observer will also make it possible to analyze the behaviour of the flux linkage harmonics in the flux-weakening region.

The inductances in the machine should be carefully measured and inductance harmonics [22, 21] and saturation phenomena [23] should be taken into account.

Methods to determine the most energy efficient current references in the whole operation region, have been developed [4, 16] and they should be implemented and validated experimentally (this requires a detailed knowledge of all machine parameters).

Regarding the sensorless algorithm, many parameters have to be set correctly, in order to get it working properly. This should be further analyzed and the proper function of the sensorless algorithm must be demonstrated in the whole operating region of the machine. The sensorless algorithm consumes reactive power which flows between the DC-link and the machine. This may increase the system losses and they should be investigated. If a resolver is mounted in the machine for HEV applications and the sensorless algorithm is used as a backup system, the sensorless algorithm must be demonstrated to work correctly during a resolver failure in the whole operating region.

Bibliography

- [1] N. Bianchi and S. Bolognani, *Innovative Design and Optimisation of Electrical Machines*, Post-Graduate seminar lecture notes, vol. 7, Helsinki University of Technology, 26/2-3/3, 2001.
- [2] I. Boldea and S. A. Nasar, *Electric Drives*, CRC Press, Boca Raton, 1999.
- [3] P. L. Chapman, S. D. Sudhoff and C. A. Whitcomb, "Multiple reference frame analysis of non-sinusoidal brushless DC drives," *IEEE Transactions on Energy Conversion*, vol. 14, no. 3, pp. 440-446, Sept. 1999.
- [4] F. Colamartino, C. Marchand and A. Razek, "Torque ripple minimization in permanent magnet synchronous servodrive," *IEEE Transactions on Energy Conversion*, vol. 14, no. 3, pp. 616-621, Sept. 1999.
- [5] M. J. Corley and R. D. Lorenz, "Rotor position and velocity estimation for a salient-pole permanent magnet synchronous machine at standstill and high speed," *IEEE Transactions on Industry Applications*, vol. 34, no. 4, pp. 784-789, July/Aug. 1998.
- [6] T. Glad and L. Ljung, *Reglerteori* (in swedish), Studentlitteratur, Lund, 1997.
- [7] L. Harnefors and H.-P. Nee, "A general algorithm for speed and position estimation of AC motors," *IEEE Transactions on Industrial Electronics*, vol. 47, no. 1, pp. 77-83, Feb. 2000.
- [8] L. Harnefors and H.-P. Nee, *Control of Variable-Speed Drives*, Royal Institute of Technology, Stockholm, Sweden, 2000.
- [9] L. Harnefors and H.-P. Nee, "Model-based current control of AC machines using the internal model control method," *IEEE Transactions on Industry Applications*, vol. 34, no. 1, pp. 133-141, Jan./Feb. 1998.
- [10] L. Harnefors, *On Analysis, Control and Estimation of Variable-Speed Drives*, Ph. D. thesis, Royal Institute of Technology, Stockholm, Sweden, 1997.
- [11] L. Harnefors, K. Pietiläinen and L. Gertmar, "Torque maximizing field weakening control: design, analysis and parameter selection," *IEEE Transactions on Industrial Electronics*, vol. 48, no. 1, pp. 161-168, Feb. 2001.
- [12] J. Hellsing, *Design and Optimization of a Permanent Magnet Motor for a Hybrid Electric Vehicle*, Lic. thesis, Chalmers University of Technology, Gothenburg, Sweden, 1998.

- [13] J. Holtz and L. Springob, "Identification and compensation of torque ripple in high-precision permanent magnet motor drives," *IEEE Transactions on Industrial Electronics*, vol. 43, no. 2, pp. 309-320, April 1996.
- [14] A. Jack, B. Mecrow and C. Weiner, "Switched reluctance and permanent magnet motors suitable for vehicle drives – a comparison," *Proceedings of the IEE Seminar on Hybrid and Fuel Cell Vehicles*, pp. 6/1-6/5, April, 2000.
- [15] T. M. Jahns and W. L. Soong, "Pulsating torque minimization techniques for permanent magnet AC motor drives – a review," *IEEE Transactions on Industrial Electronics*, vol. 43, no. 2, pp. 321-330, Feb. 1996.
- [16] C.-I. Kang and I.-J. Ha, "An efficient torque control algorithm for BLDCM with a general shape of back EMF," *Proceedings of the 24th annual Power Electronics Specialists Conference (PESC)*, pp. 451-457, 20-24 June, 1993.
- [17] H. Le-Huy, R. Perret and R. Feuillet, "Minimization of torque ripple in brushless DC motor drives," *IEEE Transactions on Industrial Applications*, vol. IA-22, no. 4, pp. 748-755, July/Aug. 1986.
- [18] W. Leonard, *Control of Electrical Drives*, Springer-Verlag, Berlin, 1996.
- [19] T. Li and G. Slemon, "Reduction of cogging torque in permanent magnet motors," *IEEE Transactions on Magnetics*, vol. 24, no. 6, pp. 2901-2903, Nov. 1988.
- [20] J. Lindström, *Development of an Experimental Permanent-Magnet Motor Drive*, Lic. thesis, Chalmers University of Technology, Gothenburg, Sweden, 1999.
- [21] A. Madani, J. P. Barbot, F. Colamartino and C. Marchand, "An observer for the estimation of the inductance harmonics in a Permanent-Magnet Synchronous Machine," *Proceedings of the IEEE International Conference on Control Applications*, pp. 517-521, Oct. 5-7, 1997.
- [22] A. Madani, J. P. Barbot, F. Colamartino and C. Marchand, "Reduction of torque pulsations by inductance harmonics identification of a permanent-magnet synchronous machine," *Proceedings of the 4th IEEE Conference on Control Applications*, pp. 787-792, 28-29 Sept. 1995.
- [23] C. Mademlis and V. G. Agelidis, "On considering magnetic saturation with maximum torque to current control in interior permanent magnet synchronous motor drives," *IEEE Transactions on Energy Conversion*, vol. 16, no. 3, pp. 246-252, Sept. 2001.
- [24] J. Malan and M. J. Kamper, "Performance of a hybrid electric vehicle using reluctance synchronous machine technology," *IEEE Transactions on Industry Applications*, vol. 37, no. 5, pp. 1319-1324, Sept./Oct. 2001.
- [25] M. Morari and E. Zafiriou, *Robust Process Control*, Prentice-Hall, New Jersey, 1989.
- [26] D. W. Novotny and T. A. Lipo, *Vector Control and Dynamics of AC Drives*, Clarendon Press, Oxford, 1996.

- [27] V. Petrović, R. Ortega, A. M. Stanković and G. Tadmor, “Design and implementation of an adaptive controller for torque ripple minimization in PM synchronous motors,” *IEEE Transactions on Power Electronics*, vol. 15, no. 5, pp. 871-880, Sept. 2000.
- [28] K. M. Rahman, B. Fahimi, G. Suresh, A. V. Rajarathnam and M. Ehsani, “Advantages of switched reluctance motor applications to EV and HEV: design and control issues,” *IEEE Transactions on Industry Applications*, vol. 36, no. 1, pp. 111-121, Jan./Feb. 2000.
- [29] M. S. Sarma, *Electric Machines*, PWS Publishing Company, Boston, 1996.
- [30] L. Springob and J. Holtz, “High-bandwidth current control for torque-ripple compensation in PM synchronous machines,” *IEEE Transactions on Industrial Electronics*, vol. 45, no. 5, pp. 713-721, Oct. 1998.
- [31] P. Vas, *Vector Control of AC Machines*, Clarendon Press, Oxford, 1990.
- [32] V. Wouk, “Hybrid electric vehicles,” *Scientific American*, no. 10, Oct. 1997.
- [33] F. A. Wyczalek, “Hybrid electric vehicles year 2000,” *Proceedings of the Energy Conversion Engineering Conference and Exhibit (IECEC) 35th Intersociety*, vol. 1, pp. 349-355, July 24-28, 2000.
- [34] E. Yamada and Z. Zhao, “Applications of electrical machine for vehicle driving system,” *Proceedings of the Power Electronics and Motion Control Conference (PIEMC)*, vol 3., pp. 1359-1364, Aug. 15-18, 2000.
- [35] K. J. Åström and B. Wittenmark, *Adaptive Control*, Addison Wesley , Massachusetts, 1995.

Appendix A

Calculation of Electrical Power in $dq0$ -coordinates

To calculate an expression for the electrical power P_e in the $dq0$ -coordinates, we start by evaluating the product of the voltage and current in these coordinates.

$$\mathbf{u}_{dq0}^T \mathbf{i}_{dq0} = \left((\mathbf{T}_{dq,ph} \mathbf{u}_{ph})^T \mathbf{T}_{dq,ph} \mathbf{i}_{ph} \right) = \left(\mathbf{u}_{ph}^T \mathbf{T}_{dq,ph}^T \mathbf{T}_{dq,ph} \mathbf{i}_{ph} \right). \quad (\text{A.1})$$

Evaluating the product $\mathbf{T}_{dq,ph}^T \mathbf{T}_{dq,ph}$ yields

$$\mathbf{T}_{dq,ph}^T \mathbf{T}_{dq,ph} = \frac{1}{9} \begin{bmatrix} 5 & -1 & -1 \\ -1 & 5 & -1 \\ -1 & -1 & 5 \end{bmatrix}. \quad (\text{A.2})$$

Plugging this expression into Equation (A.1) leads to

$$\mathbf{u}_{dq0}^T \mathbf{i}_{dq0} = \frac{\mathbf{u}_{ph}^T}{9} \begin{bmatrix} 5i_a - i_b - i_c \\ -i_a + 5i_b - i_c \\ -i_a - i_b + 5i_c \end{bmatrix}. \quad (\text{A.3})$$

Since the machine is wye-connected without a neutral connection, $i_a + i_b + i_c = 0$, which simplifies Equation (A.3) to

$$\mathbf{u}_{dq0}^T \mathbf{i}_{dq0} = \frac{6\mathbf{u}_{ph}^T}{9} \mathbf{i}_{ph} = \frac{2}{3} (u_a i_a + u_b i_b + u_c i_c). \quad (\text{A.4})$$

This means that the electrical power can be expressed as

$$P_e = \frac{3}{2} (\mathbf{u}_{dq0}^T \mathbf{i}_{dq0}). \quad (\text{A.5})$$

Appendix B

Selection of γ Parameters for the MIT Update Rule

The MIT rule uses the following parameter estimation update law

$$\frac{d\hat{i}_{q,6}}{dt} = -\gamma_1 e \frac{\partial e}{\partial \hat{i}_{q,6}}, \quad (\text{B.1})$$

$$\frac{d\hat{\varphi}}{dt} = -\gamma_2 e \frac{\partial e}{\partial \hat{\varphi}}. \quad (\text{B.2})$$

γ_1 and γ_2 are parameters that have to be set and e is given as

$$e = i_{q,6} \cos(6\theta + \varphi) - \hat{i}_{q,6} \cos(6\theta + \hat{\varphi}). \quad (\text{B.3})$$

Evaluating Equations (B.1)–(B.2) leads to the following expressions where $\dot{\hat{i}}_{q,6}$ and $\dot{\hat{\varphi}}$ denote the time derivative of each parameter (note that the approximation $\theta \approx \omega_r t$ is used).

$$\dot{\hat{i}}_{q,6} = e\gamma_1 \cos(6\omega_r t + \hat{\varphi}), \quad (\text{B.4})$$

$$\dot{\hat{\varphi}} = -e\gamma_2 \hat{i}_{q,6} \sin(6\omega_r t + \hat{\varphi}). \quad (\text{B.5})$$

Linearizing these two equations around the point $\hat{\varphi} = \varphi$ and $\hat{i}_{q,6} = i_{q,6}$ yields the linearized matrix \mathbf{A}

$$\mathbf{A} = \begin{bmatrix} \frac{\partial \dot{\hat{i}}_{q,6}}{\partial \hat{i}_{q,6}} & \frac{\partial \dot{\hat{i}}_{q,6}}{\partial \hat{\varphi}} \\ \frac{\partial \dot{\hat{\varphi}}}{\partial \hat{i}_{q,6}} & \frac{\partial \dot{\hat{\varphi}}}{\partial \hat{\varphi}} \end{bmatrix}_{(\hat{\varphi}=\varphi, \hat{i}_{q,6}=i_{q,6})} \quad (\text{B.6})$$

Calculating this matrix yields

$$\mathbf{A} = \begin{bmatrix} -\gamma_1 \cos^2(6\omega_r t + \varphi) & \gamma_1 i_{q,6} \sin(6\omega_r t + \varphi) \cos(6\omega_r t + \varphi) \\ \gamma_2 i_{q,6} \sin(6\omega_r t + \varphi) \cos(6\omega_r t + \varphi) & -\gamma_2 i_{q,6}^2 \sin^2(6\omega_r t + \varphi) \end{bmatrix}. \quad (\text{B.7})$$

To analyze the stability of this linearized system we compute the characteristic polynomial

$$\det(s\mathbf{I} - \mathbf{A}) = \frac{s}{2} (\gamma_1 + \gamma_2 i_{q,6}^2 + 2s + (\gamma_1 - \gamma_2 i_{q,6}^2) \cos(2(6\omega_r t + \varphi))). \quad (\text{B.8})$$

To simplify the equations we set $\gamma_1 = \gamma_2 = \gamma$. This yields

$$\frac{s}{2}(\gamma + \gamma i_{q,6}^2 + 2s + (\gamma - \gamma i_{q,6}^2) \cos(2(6\omega_r t + \varphi))). \quad (\text{B.9})$$

This is an algebraic second order equation in s and the solution is $s_1 = 0$ and

$$s_2 = -\frac{\gamma}{2}(1 - \cos(12\omega_r t + 2\varphi)) - \frac{\gamma i_{q,6}^2}{2}(1 - \cos(12\omega_r t + 2\varphi)). \quad (\text{B.10})$$

We can see that $s_2 \leq 0$. The solution, $s_1 = 0$, means that the estimator has one pole in origo which can lead to oscillatory behaviour.

Appendix C

Laboratory Setup Data

This appendix contains a list of important parameters of the laboratory setup used in this thesis (both in the implementations and simulations). See [12, 20] for a more complete description. The parameters denoted by an asterisk (*) have been measured by the author during this thesis project.

Motor data

Parameter	Value
Type	Permanent magnet synchronous machine
Rotor magnet material	NeFeB
Base speed	$\omega_{r,\text{base}} = 1257 \text{ rad/s} \Leftrightarrow n_{\text{base}} = 6000 \text{ rpm}$
Maximum speed	$n_{\text{max}} = 12000 \text{ rpm}$
Rated current	160 A
Rated voltage (line-to-line)	220 V
Number of pole pairs	$n_p = 2$
d -axis inductance	$L_d = 0.2 \text{ mH}$
q -axis inductance	$L_q = 0.5 \text{ mH}$
Armature resistance	$R_s = 13 \text{ m}\Omega/\text{phase}$
Fundamental flux linkage*	$\Psi_m = 103.9 \text{ mWb}$
6:th harmonic in flux linkage, d-axis*	$\Psi_{d6} = 2.30 \text{ mWb}$
12:th harmonic in flux linkage, d-axis*	$\Psi_{d12} = 0.26 \text{ mWb}$
18:th harmonic in flux linkage, d-axis*	$\Psi_{d18} = 0.57 \text{ mWb}$
6:th harmonic in flux linkage, q-axis*	$\Psi_{q6} = 6.22 \text{ mWb}$
12:th harmonic in flux linkage, q-axis*	$\Psi_{q12} = 1.60 \text{ mWb}$
18:th harmonic in flux linkage, q-axis*	$\Psi_{q18} = 2.04 \text{ mWb}$

Drivetrain data

Parameter	Value
Loading machine	DC machine connected through a reduction gearbox
Moment of inertia*	$J = 168.9 \cdot 10^{-3} \text{ kgm}^2$
Friction coefficient*	$B_{\text{fric}} = 2.36 \text{ kgm}^2/\text{s}, -50 \leq \omega_r \leq 50 \text{ rad/s}$.
Reduction gearbox ratio	3.09 : 1

DSP data

Parameter	Value
DSP Model	TMS320C30
Sampling frequency	$f_s = 5.859$ kHz

VSI data

Parameter	Value
Transistor type	IGBT
Switching frequency	$f_{sw} = 5.859$ kHz
Maximum DC-link voltage	450 V
Maximum collector current	600 A

Appendix D

Pictures of Laboratory Setup

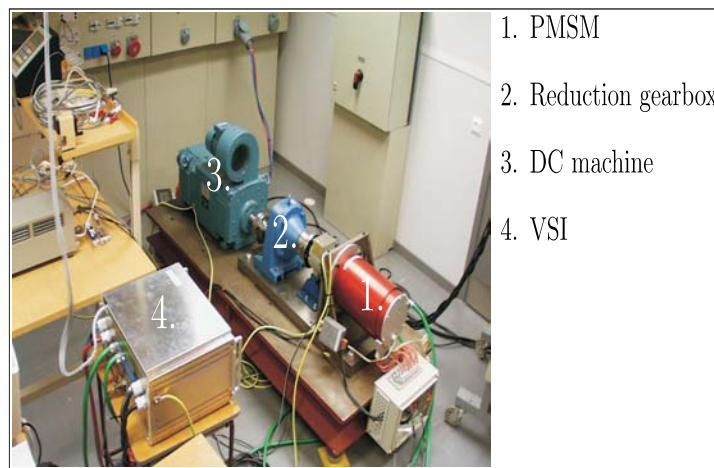


Figure D.1: Picture of total laboratory setup.

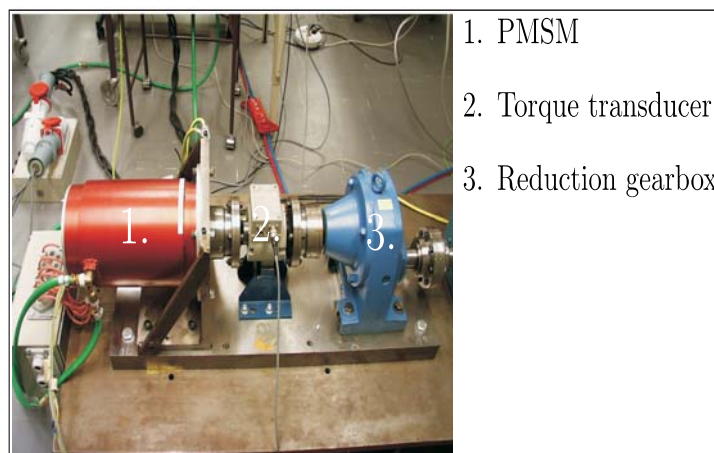


Figure D.2: Close view of PMSM.

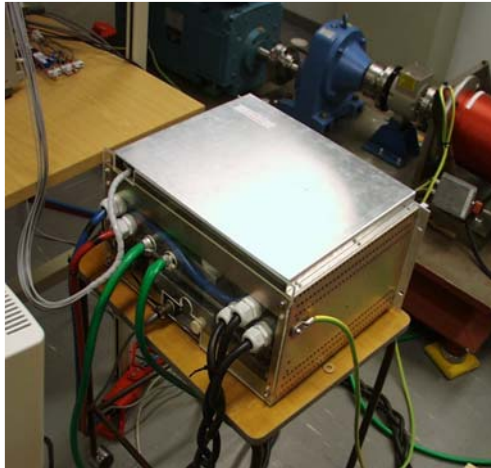


Figure D.3: Picture of the voltage source inverter.

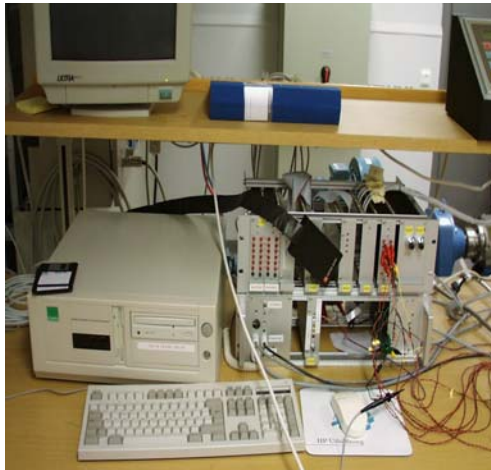


Figure D.4: DSP-system with control computer.